

Chapter 2

Computer Modeling of Transport Layer Effects

André Richter

Abstract This chapter introduces the reader into optical signal representations and the major physical layer effects causing system degradations in the WDM transport layer. Suitable modeling approaches are presented, and typical simulation results are demonstrated. Finally, the chapter focuses on performance degrading effects due to fiber propagation, optical amplification, and signal generation.

2.1 The Value of System-Level Simulation

System-level simulations are now routinely used to theoretically evaluate the performance of transmission systems based on the parameters of existing optical equipment, and to define performance requirements for new equipment to ensure robust operation for all required application scenarios. In a sense, system simulation is used as a virtual prototyping tool that reduces cost by shortening the system construction cycle. Furthermore, simulations prove valuable for investigating possible upgrade scenarios, understanding the nature and sources for system-limiting effects, determining the full effect of component limitations, and developing new technological approaches. The most critical part in designing accurate and reliable system simulation scenarios is selection of the right parameters and accurate transport effect models.

A. Richter (✉)
VPIphotonics Division, VPIsystems
Berlin, Germany
e-mail: Andre.Richter@VPIphotonics.com

2.2 Simulation Domains and Signal Representations

For computer simulation to be effective, optical signals need to be represented into the computer. Optical signal representations with different degrees of abstraction are important in providing flexibility for modeling various aspects of photonic networks. Since the initial publications of the fundamental concept as in Lowery et al. [1], many improvements have been introduced supporting the modeling requirements of the ever-evolving advances in optical technologies and network architectures [2].

Time-domain simulations that propagate individual time samples on an iteration-by-iteration basis between modeling blocks have been used to investigate, for instance, the properties of integrated photonic circuits, high-speed transmitters, and receivers, where the analysis of bidirectional interactions in the picoseconds range are of key importance [3]. For optical systems and networking applications mixed-domain simulations (i.e. including both, the time- and frequency-domains) are more suitable where arrays of signal samples are passed between modeling blocks. Applications are mainly unidirectional propagation scenarios and bidirectional scenarios where time delays are longer than the array duration (e.g., optical switching scenarios in bidirectional ring networks), or where bidirectional interactions can be averaged in time (e.g., bidirectional Raman pumping of optical fiber).

The simulation efficiency of mixed-domain simulations can be controlled by representing optical signals either by their complex, polarization-dependent sampled waveform (time-dynamic or spectral representation), or by time-averaged parameters only. Depending on the modeling scope of interest, the time-dynamic representation can be applied to a single frequency band (SFB), or to multiple (non-overlapping) frequency bands (MFBs) for which the appropriate propagation equations describe the evolution of individual frequency bands, while interacting terms are approximated using frequency decomposition (FD) techniques.

Although waveform-dependent propagation effects are ignored when using a parameterized representation of optical signals, this approach provides significant simulation speed-up while keeping sufficient modeling accuracy when investigating, for instance, the impact of ‘far-away’ WDM channels or optical pumps. Parameterized Signals (PS) can also be used to track important properties along the transmission path such as power, principal states of polarization (PSP), as well as accumulated amounts of noise, chromatic dispersion (CD), self-phase modulation (SPM), differential group delay (DGD), and thus easily assess signal characteristics over topology and frequency. Additive noise that is generated by lumped or distributed optical amplifiers can be tracked separately from the optical signal, disregarding nonlinear interaction effects between noise and signal, or accounting for them at the receiver using deterministic system performance estimation algorithms. In that case, optical noise can be described by its wavelength-dependent power spectral density (PSD), which could be step-wise approximated by so-called Noise Bins (NBs) of constant PSD. Further on, the parameterized representation is useful for keeping parasitic terms resulting from optical amplification, crosstalk,

and scattering processes (collectively called Distortions) separate from the optical signal, and thus, allowing the investigation of their impact on the signal quality.

2.3 Device Modeling

Different levels of abstraction in device modeling help to address the tradeoffs between the model complexity, simulation accuracy and computation speed [4] thus allowing the researcher to choose the required depth of detail. Typically, detailed models require in-depth parameters, whereas behavioral models operate on measured characteristics, or information from data sheets. At one extreme, detailed physical models represent components based on material and structural parameters. These parameters may be difficult to obtain, being proprietary, or difficult to derive from external measurements of a packaged device. Detailed physical models may require intensive computation, but can be used to design new devices and predict their performance. Black-box models are based on the physics of the device, but can be described in terms of behavioral parameters (instead of in-depth parameters), which can be directly derived from external measurements. Linear devices (such as filters) or well-specified devices (such as transmitters with a digital input) can be represented by their measured performance alone. Although novel devices cannot be designed directly using these models, the system performance of a module is easily and accurately assessed using these methods. Data sheets often provide characteristics as a series of parameters fitted to measurements (such as rise-time, spectral width). Although such data are often gathered using long-term measurements, their wide availability makes it useful for systems-level simulation. Attention should be given so that long-term averages do not misrepresent the worst case.

2.4 Fiber Propagation

Transmission effects influencing signal propagation over single-mode optical fiber can be grouped into several general categories arising from the fiber properties itself. There are first optical power loss effects, which are either regarded as being equally distributed along the fiber distance (e.g., power attenuation) or occur at isolated points along the fiber due to discrete events such as splices and fiber ends. Further on, the velocity of light traveling through the fiber depends on the wavelength, which results into dispersive effects of information-carrying optical signals. The so-called group velocity dispersion (or CD) is a linear propagation effect, which could theoretically be reversed after fiber propagation by means that are independent of the transmitted signal, for example, using components with opposite dispersion such as using dispersion compensating fiber (DCF) or fiber

Bragg gratings (FBG). Additionally, power loss and dispersive propagation effects might be dependent on the local polarization state in time and frequency due to manufacturing imperfections, stress or other effects changing the properties of the perfectly circular optical single-mode fiber. Important effects are polarization mode dispersion (PMD) and polarization-dependent loss/gain (PDL/PDG).

In addition to the above-mentioned linear effects linear scattering processes such as Rayleigh scattering, spontaneous Raman- and Brillouin- scattering are also important to consider. Rayleigh scattering can be understood as distributed reflection of the light wave on microscopic in-homogeneities of the fiber medium. This effect significantly contributes to the fiber loss. Furthermore, double Rayleigh scattering leads to a reflected lightwave propagating in the same direction as the originating signal and therefore interferes with it. While the reflection strength is typically small, the effect may become significant in high amplifying media (for instance Raman amplifiers with high pump power). Spontaneous Brillouin and Raman scattering effects are caused by the scattering of the lightwave on thermally induced acoustic waves or molecular oscillations of the fiber medium (also referred to as acoustic and optical phonons, respectively). The importance of these effects results from the fact that the spontaneously scattered signal becomes a seed for further amplification by the much stronger nonlinear (stimulated) scattering effects, which are considered below.

Besides polarization-independent or dependent linear effects, signal transmission over optical fiber may suffer from effects, which result from the nonlinear interactions of the fiber material and the light traveling through it. Nonlinear propagation effects can generally be categorized as effects involving instantaneous or almost instantaneous electronic contributions—the optical Kerr effect and its various manifestations as SPM, cross-phase modulation (XPM), and four-wave mixing (FWM) as well as nonlinear effects with a noticeable time response: stimulated Brillouin and Raman scattering (SBS and SRS) respectively. Depending on the response time the spectral bandwidth of these nonlinear effects varies from almost unlimited (in telecommunications terms) for the Kerr effect, intermediate for the Raman effect (in the vicinity of 13 THz) and rather small for the Brillouin effect (linewidth of about 100 MHz and a Stokes shift of about 10 GHz).

Finally, it is important to note that the nonlinear propagation effects occur in coexistence to CD, polarization effects, and attenuation, and may produce complex degradations or beneficial interactions (depending on the system parameters under investigation). For example, the FWM efficiency depends strongly on the CD of the fiber; SPM can support very stable pulse propagation in the presence of the right amount of CD; the impact of PMD can be reduced by nonlinear fiber interactions; the polarization dependence of SRS may introduce PDG. Thus, accurate fiber modeling needs to include nonlinear and linear phenomena, so that detrimental and beneficial interactions between these characteristics are predicted correctly.

2.4.1 Linear Propagation Effects

2.4.1.1 Attenuation

Fiber attenuation is mainly caused by absorption and scattering processes. It determines the resulting exponential decay of optical input power propagating through the fiber. Absorption arises from impurities and atomic effects in the fiber glass. Scattering is mainly due to intrinsic refractive index variations with distance (Rayleigh scattering) and imperfections of the cylindrical symmetry of the fiber. The usable bandwidth ranges from approximately 800 nm (increased Rayleigh scattering scales with λ^{-4} [5, 6]) to approximately 1,620 nm (infrared absorption due to vibrational transitions). Older types of single-mode fiber show additionally an attenuation peak at approximately 1,400 nm due to the absorption of water molecules.

Typically being specified in logarithmic units as dB/km, sometimes it is useful to work with attenuation values in linear units so:

$$\alpha = \left(\frac{\log_e(10)}{10} \right) \alpha_{\text{dB/km}} \approx 0.23026 \alpha_{\text{dB/km}} \quad (2.1)$$

For single channel applications α can be assumed to be wavelength-independent. However, for applications covering a large spectral range, such as multi-band WDM or Raman amplification, the spectral dependency of fiber attenuation should be accounted for accurately in simulations.

The effective length L_{eff} defines the equivalent fiber interaction length with respect to constant power [7] so that:

$$L_{\text{eff}} = \int_0^z e^{-\alpha z_1} dz_1 = \frac{1 - e^{-\alpha z}}{\alpha} \quad (2.2)$$

In the above, L_{eff} is an important quality measure when rescaling the signal evolution to account for attenuation and periodic amplification, and helpful when performing quick system performance estimations.

2.4.1.2 Chromatic Dispersion

The CD or group velocity dispersion (GVD) represents a fundamental linear propagation limitation in optical fiber. It describes the effect that different spectral components propagate with different group velocities. CD alone causes spreading of chirp-less pulses along the fiber, although this statement is not true in general. For instance, in combination with nonlinear propagation effects other pulse propagation characteristics are detectable. Note that CD is a collective effect of material and waveguide dispersion [6, 8]. Depending on the manufacturing process and the radial structure of the fiber, different fiber types with various CD profiles can be designed. In standard single-mode fibers (SSMF) the GVD is positive (i.e. shorter wavelengths propagate faster) for wavelengths longer than

approximately 1.3 μm and negative for shorter wavelengths. Thus, 1.3 μm is the point of zero GVD for SMFs. The fiber design allows shifting the point of zero dispersion and production of zero-dispersion fibers at 1.5 μm called dispersion-shifted fibers (DSF) or fibers with low positive or negative dispersion at that wavelength called non-zero dispersion-shifter fibers (NZ-DSF), as well as fibers with high negative dispersion values for dispersion compensation called DCF.

The impact of GVD on pulse propagation becomes clearer when expanding the modal propagation constant $\beta(\omega)$ in a Taylor series around an arbitrary frequency ω_0 as shown in Agrawal [9]:

$$\beta(\omega) = n(\omega) \frac{\omega}{c} = \beta_0 + \beta_1(\omega - \omega_0) + \frac{1}{2}\beta_2(\omega - \omega_0)^2 + \frac{1}{6}\beta_3(\omega - \omega_0)^3 \quad (2.3)$$

where $n(\omega)$ is the effective refractive index of the fiber, c is the speed of light in a vacuum, and $\beta_k = \partial^k / \partial \omega^k \beta(\omega)$ at $\omega = \omega_0$ for $k = 0, 1, 2, 3$ (i.e. partial derivative of $\beta(\omega)$ with respect to ω evaluated at ω_0)

In the above:

- β_0 accounts for a frequency-independent phase offset during propagation corresponding to the propagation constant at a certain reference frequency.
- β_1 defines the inverse of the group velocity v_g determining the speed of energy propagated through the fiber.
- β_2 defines the GVD and describes the frequency dependence of the inverse of v_g . It is responsible for the broadening of an initially chirp-less pulse due to the fact that its Fourier components propagate with different group velocities. This also leads to pulse chirp when the leading and trailing edges of the pulse contain light with different frequencies. Equivalently, it defines the different propagation speeds of pulses in frequency-separated channels (such as in WDM systems).
- β_3 is known as the slope of the GVD or second order GVD. This term accounts for the frequency dependence of the GVD and therefore for the different broadening properties of signals or signal portions propagating at different frequencies. This term is critical for wideband transmission systems, for systems operating in frequency regions where β_2 is close to zero as well as systems utilizing DCFs to compensate dispersion for multiple WDM channels simultaneously.

In general, it is of more interest to determine the dependence of the inverse of the group velocity v_g on wavelength rather than on frequency. This dependence is described by the dispersion parameter D and its slope with respect to wavelength, S . The following relationships inter-relate the above parameters:

$$D = \frac{d}{d\lambda} \frac{1}{v_g} = -\frac{2\pi c}{\lambda^2} \beta_2 \quad (2.4)$$

$$S = \frac{dD}{d\lambda} = \frac{(2\pi c)^2}{\lambda^3} \left(\frac{1}{\lambda} \beta_3 + \frac{1}{\pi c} \beta_2 \right) \quad (2.5)$$

$$\beta_2 = \frac{d}{d\omega} \frac{1}{v_g} = -\frac{\lambda^2}{2\pi c} D \quad (2.6)$$

$$\beta_3 = \frac{d\beta_2}{d\omega} = \frac{\lambda^3}{(2\pi c)^2} (\lambda S + 2D) \quad (2.7)$$

D is typically measured in ps/nm-km and can be interpreted as describing the broadening ΔT of a pulse with bandwidth $\Delta\lambda$ after propagation over a distance z , or equivalently, the time offset ΔT of two pulses after distance z that are separated in the spectral domain by $\Delta\lambda$.

ΔT is given below as:

$$\Delta T \approx \Delta\lambda \frac{dT}{d\lambda} = \Delta\lambda z \frac{d}{d\lambda} \frac{1}{v_g} = \Delta\lambda z D \quad (2.8)$$

From the above, the walk-off length L_w can be defined as the distance it takes for one pulse with duration T_0 traveling at frequency ω_1 to overtake another pulse traveling at frequency ω_2 and is thus given by:

$$L_w = \frac{T_0}{|\beta_1(\omega_2) - \beta_1(\omega_1)|} \approx \frac{T_0}{|\Delta\lambda D|} \quad (2.9)$$

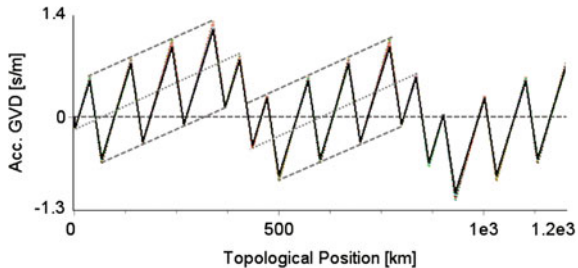
The dispersion length L_D characterizes the distance over which dispersive effects become important in the absence of other effects. Specifically, it defines the distance over which a chirp-free Gaussian pulse broadens by a factor of $\sqrt{2}$ due to GVD and is given by:

$$L_D = \frac{T_0^2}{|\beta_2|} = \frac{2\pi c}{\lambda^2} \frac{T_0^2}{|D|} \quad (2.10)$$

However, L_D can also be applied as an approximation to determine the relevance of CD effects on other intensity modulated pulses. Since L_D is inversely proportional to the square of the signal bandwidth, as an example, the CD requirement increases by a factor of 16 when increasing the signal bitrate from 10 to 40 Gbit/s using the same modulation format and filter bandwidths that are proportional to the signal rate. In consequence, CD limits uncompensated 40 Gbit/s NRZ transmission over SSMF to approximately 4 km and over NZ-DSF to approximately 20 km. Additional dispersion variations due to changes in temperature along the link accumulate fluctuations as shown in Kato et al. [10] that have to be compensated adaptively, especially in long-haul applications.

So it would be natural to think that low- or zero-dispersion fibers are the optimum choice for WDM systems design. However, instead of using DSFs with very small local GVD values, it is more appropriate to use transmission fibers with larger local dispersion values (e.g., SSMF or NZ-DSF) and place DCFs at regular distances along the link compensating for all or part of the accumulated CD the optical signal experienced up to that point. If optical fiber were a purely linear

Fig. 2.1 Dispersion management for a long-haul transmission experiment where dispersion compensation is placed at regular intervals along the fiber as described in Liu et al. [11]



transmission medium it would not matter at which point along the link CD is compensated. However, as will be described in the following section, fiber propagation is slightly dependent on the intensity of the light traveling through it, thus resulting in nonlinear propagation effects. In modern WDM transmission systems with channel symbol rates of 10 Gbit/s and beyond, dispersion management taking care of the careful adjustment of local CD values (not too small) and maximum accumulated CD before dispersion compensation (not too large) helps to control these nonlinear fiber impairments (Fig. 2.1).

2.4.2 Nonlinear Propagation Effects

2.4.2.1 Kerr Effect

The Kerr effect denotes the phenomenon in which the refractive index of an optical fiber $n(\omega, t)$ is slightly dependent on the intensity of the optical signal $I(t) = |E(t)|^2$, with $E(t)$ being the electric field, passing through the fiber. As a result:

$$n(\omega, t) = n_0(\omega) + n_2 I(t) \quad (2.11)$$

where n_0 is the linear refractive index and n_2 is the nonlinear refractive index of the fiber.

When the electric field intensity of the transmitted signal bit stream varies in time it induces an intensity-dependent modulation of the refractive index, and hence, modulation of the phase of the transmitted signal. Compared to other nonlinear media, n_2 is very small (typically on the order of 10^{-20} [m²/W]). However, even this weak fiber nonlinearity becomes fairly relevant for signal propagation as field intensities of several mWs are focused in a small fiber core (in the order of several tens of μm^2) over interaction lengths of tens to hundreds of kilometers. As a result, effects such as nonlinear interaction between signal pulses might accumulate during transmission and become of system limiting importance.

In conclusion, the Kerr nonlinearity results in several intensity-dependent propagation effects, with the most important ones being SPM, XPM, and FWM.

Self- and Cross-Phase Modulation

SPM and XPM occur when a temporal variation of the optical signal intensity induces a temporal phase shift on the originating signal (SPM) or on other co-propagating signals at different wavelengths (XPM).

For example, in the case where several optical signals at different wavelengths each with intensity $I(t)$ and initial phase φ_0 are launched into a fiber, the phase modulation of the signal corresponding to channel m depends on the local power distribution of all other channels as follows:

$$\begin{aligned}\varphi_m(t, z) - \varphi_{0,m} &= \varphi_{lin,m} + \varphi_{SPM,m} + \varphi_{XPM,m} \\ &= \frac{2\pi}{\lambda} n_{0,m} z + \frac{2\pi}{\lambda} n_2 z I_m(t) + \frac{4\pi}{\lambda} n_2 z \sum_{k \neq m} I_k(t)\end{aligned}\quad (2.12)$$

where $\varphi_m(t, z)$ is the phase modulation of channel m , $\varphi_{0,m}$ is the initial phase of channel m , $n_{0,m}$ is the linear refractive index of channel m , n_2 is the nonlinear refractive index, and k is an index denoting the neighboring WDM channels of channel m .

Furthermore:

- $\varphi_{lin,m}$ corresponds to the accumulated linear phase shift due to transmission.
- $\varphi_{SPM,m}$ corresponds to the accumulated nonlinear phase shift due to SPM in channel m . The SPM-induced phase shift is proportional to the local signal intensity. It induces chirp (time-varying frequency shift) and spectral broadening, so as an example, pulses behave differently in the presence of GVD and optical filtering.
- $\varphi_{XPM,m}$ corresponds to the accumulated nonlinear phase shift due to XPM in channel m describing the phase modulation that is induced by intensity fluctuations in neighboring WDM channels. XPM introduces additional nonlinear phase shifts that interact with the local dispersion as well.

It must be noted that XPM occurs only over distances where optical intensities at different frequency components co-propagate, e.g. pulses propagating in different WDM channels are overlapping. In general, the XPM effect reduces with increased CD as pulses at different frequencies propagate faster through each other, e.g. L_w (as defined in [Sect. 2.4.1.2](#)) becomes smaller. For the same reason, XPM scales inversely with the channel spacing. L_w is also called the collision length L_c as it accounts for the distance where two pulses at different frequencies collide (and thus, interact nonlinearly due to XPM) during propagation.

Four-Wave Mixing

Parametric interactions between optical field intensities at different frequencies might induce the generation of inter-modulation products at new frequencies when propagating optical signals over wide spectral ranges through the fiber.

This nonlinear effect is called FWM. FWM can occur between channels in WDM systems, between optical noise and channels, and between the tones within one channel. More generally noted, FWM occurs for instance when two photons at frequencies ω_1 and ω_2 are absorbed to produce two other photons at frequencies ω_3 and ω_4 satisfying the relation below:

$$\omega_1 + \omega_2 = \omega_3 + \omega_4 \quad (2.13)$$

It could also be understood as mixing of three waves producing a fourth one according to the electrical field equations below:

$$\begin{aligned} E_{klm} &= E_k E_l E_m^* \\ &= |E_k| |E_l| |E_m| e^{j(\omega_k + \omega_l - \omega_m)t} e^{-j[\beta(\omega_k) + \beta(\omega_l) - \beta(\omega_m)]z} \end{aligned} \quad (2.14)$$

where E_i is the electric field of the wave propagating at frequency ω_i , $\beta(\omega_i)$ is the modal propagation constant at ω_i , and $\omega_{klm} = \omega_k + \omega_l - \omega_m$ is the carrier frequency of E_{klm} . The energy of E_{klm} is given as the superposition of mixing products of any three waves for which $\omega_{klm} = \omega_k + \omega_l - \omega_m$ holds (with the degenerate case for $\omega_k = \omega_l$). Note that the propagation constant is frequency-dependent, so efficient interactions only occur if contributions to E_{klm} given at different times add up over distance, e.g., the phase mismatch $\Delta\beta$ between the inter-modulating fields tends to go to zero (phase matching condition):

$$\Delta\beta \rightarrow 0, \quad \Delta\beta(\omega) = \beta(\omega_k) + \beta(\omega_l) - \beta(\omega_m) - \beta(\omega_{klm}) \quad (2.15)$$

The power of the newly created wave is proportional to the power of the three interacting waves assuming no pump depletion due to FWM occurs [12] resulting in:

$$I_{klm}(z) = |E_{klm}(z)|^2 = \eta^2 \gamma_{klm}^2 |E_k(z)|^2 |E_l(z)|^2 |E_m(z)|^2 e^{-\alpha z} L_{\text{eff}}^2 \quad (2.16)$$

where γ_{klm} is the nonlinear index of the fiber at ω_{klm} , α is the fiber attenuation, z is the propagation distance, L_{eff} is the effective length, and η is the so-called FWM efficiency given by:

$$\eta = \frac{\alpha^2}{\alpha^2 + \Delta\beta} \frac{1 + 4e^{-\alpha z} \sin^2(\Delta\beta z/2)}{(1 - e^{-\alpha z})^2} \quad (2.17)$$

FWM between the WDM channels scales inversely with channel spacing in case of non-zero GVD. Increasing the local dispersion results in an increased walk-off of the Fourier components and thus, it results in phase mismatch after shorter propagation distances, which leads to an even steeper decrease of the FWM efficiency with channel separation.

Fig. 2.2 presents the results of a case study where four 10 Gbit/s NRZ signals are propagated over 50 km of DSF and NZ-DSF fiber segments, respectively. Figure 2.2a shows the spectrum after transmission over 10 km of DSF, while Fig. 2.2b shows the corresponding spectrum after transmission over 10 km of

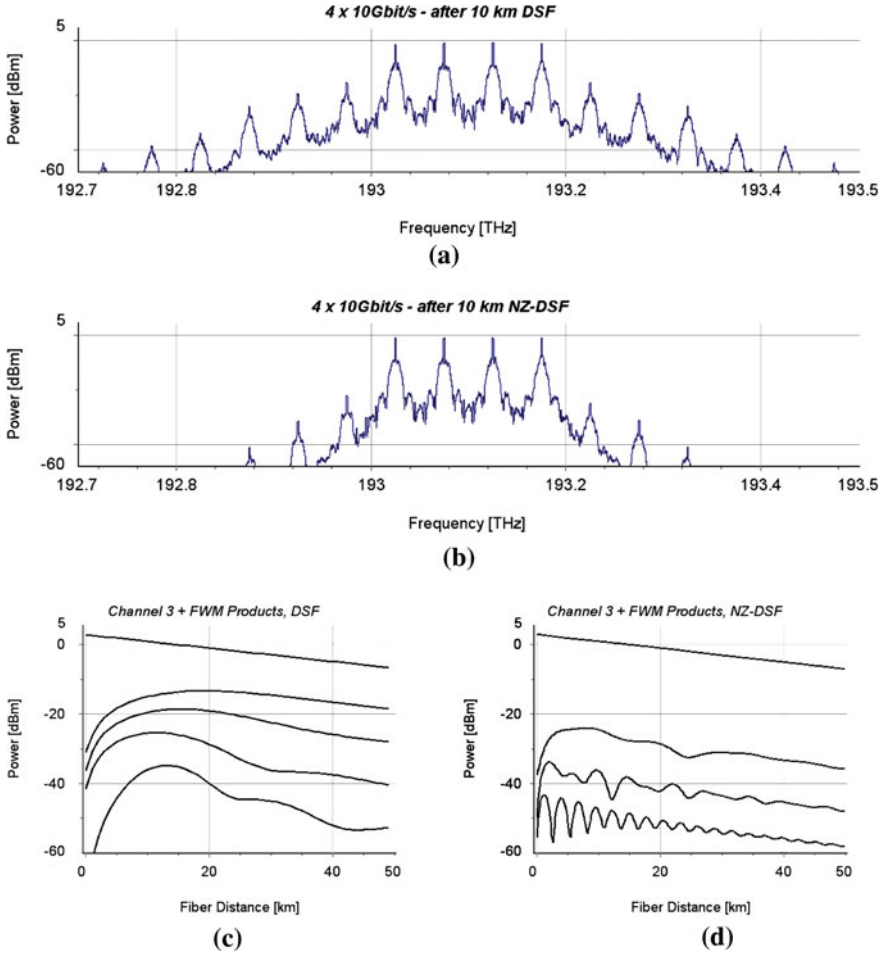


Fig. 2.2 Spectrum of four 10 Gbit/s NRZ channels after transmission over 10 km of: **a** DSF; **b** NZ-DSF segments. Power profiles of channel 3 with FWM products for propagation over: **c** DSF; **d** NZ-DSF segments

NZ-DSF. The larger local dispersion of the NZ-DSF with respect to the DSF results in an increased walk-off between the interacting tones (e.g., WDM channels and FWM distortions outside the WDM spectrum that are created during propagation). Hence, the FWM efficiency is reduced resulting in mixing products of lower power and faster power oscillations during propagation. This can be observed when comparing Fig. 2.2c showing the power levels of channel 3 and the FWM products versus DSF distance and Fig. 2.2d showing the power profiles for the corresponding NZ-DSF case.

The number of generated FWM components that are created when signals at N wavelengths mix together grows with $N^2(N-1)/2$. Using a sampled signal representation, all important components that fall into the simulation bandwidth are automatically included when solving the fiber propagation equations (see Sect. 2.4.4.1). Note that the simulation bandwidth should be chosen wide enough in order to avoid misleading results due to aliasing effects of the generated FWM components [13].

When accounting for FWM distortions using parametric modeling, the number of calculated FWM components shall be limited to avoid excessive numerical effort by considering only FWM distortions that would reach a certain power threshold, and thus, are important to be accounted for in system performance analysis.

Kerr Nonlinearities and CD

Similar to the dispersion length L_D , a scale length for Kerr nonlinearities in optical fiber could be defined: the nonlinear length L_{NL} is given as the distance over which the phase of a pulse with intensity I changes by one rad due to the Kerr nonlinearity in a fiber with a nonlinear coefficient γ

$$L_{NL} = \frac{1}{\gamma I^2} \quad (2.18)$$

L_{NL} denotes the distance where nonlinear effects become important (in the absence of other effects), also called nonlinear scale length. The ratio between L_D and L_{NL} describes the dominating behavior for signal evolution in optical fiber. For $L_D < L_{NL}$ linear effects dominate the signal propagation. In these quasi-linear systems pulse powers change rapidly in time due to dispersion-induced pulse spreading and compression over L_{NL} , and thus, the impact of nonlinear propagation effects is averaged [14]. Those nonlinear pulse-to-pulse interactions can be best described by time-equivalent terms of FWM and XPM, namely intra-channel four-wave mixing (I-FWM) and intra-channel cross-phase modulation (I-XPM) as described in Essiambre et al. [15], Mamyshev and Mamyshev [16]. Typically, I-FWM induces pulse echoes while I-XPM induces timing jitter. Pulse-to-pulse interactions in quasi-linear systems become important for bitrates of 40 Gbit/s and higher. With a careful selection of launch power, pre-chirp as well as the dispersion map, degradations due to I-XPM and I-FWM can be drastically reduced (see for instance [17–19]).

Of special interest is also the case when $L_D \sim L_{NL}$. In these nonlinearity-supporting systems cancelation of dispersive and nonlinear effects can be observed for carefully chosen system settings such as in soliton or dispersion-managed soliton (DMS) systems. Choosing system parameters such as pulse width, separation, power, as well as dispersion map and amplifier position and separation carefully, pulse chirp introduced by CD and SPM may combine and be used

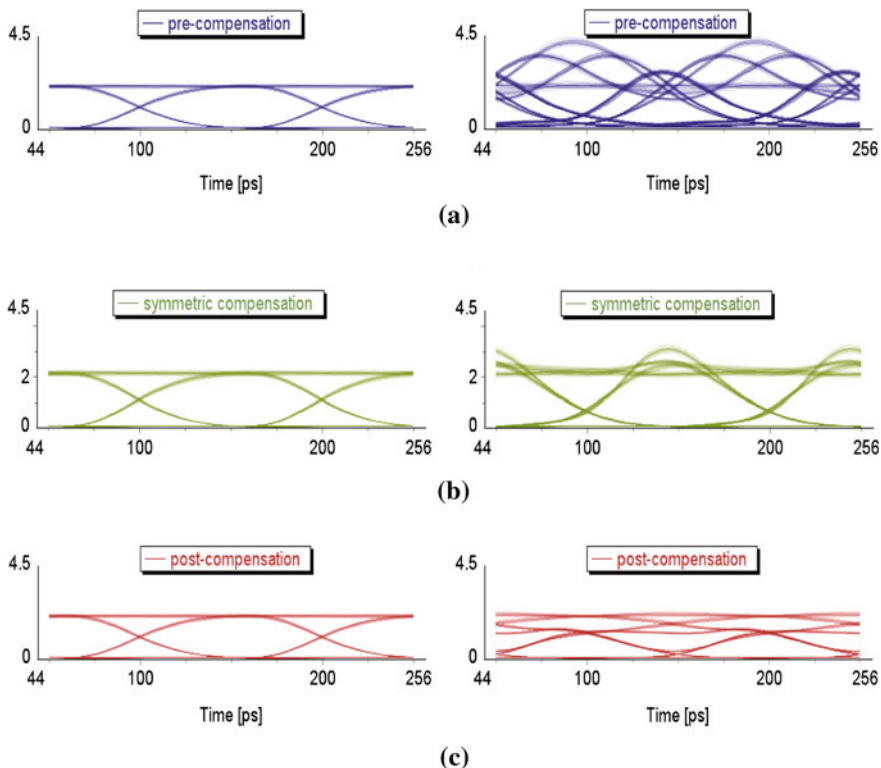


Fig. 2.3 Eye diagrams of a 10 Gbit/s NRZ signal after propagation over four spans of 80 km SSMF for three different dispersion compensation schemes: **a** pre-compensation; **b** symmetric compensation; **c** post-compensation. For each case, eye diagrams without consideration of Kerr nonlinearities are displayed on the *left* and including Kerr nonlinearities on the *right*

advantageously for stabilizing pulse propagation over very long distances. However, XPM introduces timing jitter, which in addition to timing jitter induced by added optical noise along the link is one of the ultimate limitations for such systems (see for instance [20]).

Fig. 2.3 shows results of a single channel 10 Gbit/s NRZ transmission over four spans of 80 km SSMF using different methods of dispersion compensation. Figure 2.3a shows eye diagrams (with and without considering Kerr nonlinearities) for the case that 100% of the accumulated dispersion of each SSMF span is compensated before entering the fiber (pre-compensation). Figure 2.3b shows the corresponding results when applying symmetrical compensation, e.g., equal parts of dispersion compensation are performed before and after the SSMF. Figure 2.3c shows the eye diagrams when the accumulated dispersion of each SSMF span is compensated after the fiber (post-compensation). Appropriate DCMs are placed at mid-stage access EDFAs before and/or after each span, which also set the signal

power into the transmission fiber at 10 dBm. Admittedly this value is rather large, though, it is chosen here in order to demonstrate the importance of considering Kerr nonlinearities when designing for an optimum dispersion map and amplifier placement.

2.4.2.2 Scattering Effects

Stimulated Raman Scattering

Stimulated Raman scattering (SRS) is one of the most important scattering effects in optical fiber. It denotes the inelastic process in which light is scattered by material scattering centers, which causes vibrational excitation of molecules. As a result, energy is lost to the material with the effect that lower energy photons are created from higher energy photons. Effectively, this means that signals at shorter wavelengths are attenuated and signals at longer wavelength are amplified. SRS has an important application for WDM systems, as relatively high distributed amplifications may be achieved over the length of the transmission fiber. However, it may also induce the Raman-induced tilt of WDM channel powers when the shorter wavelength channels become attenuated at the expense of longer wavelength channels.

Raman scattering is present at all optical frequencies, e.g., Raman amplification can be achieved at any wavelength (if an appropriate pump is available). The amplification range using a single pump wavelength is broadband (about 6 THz at 1.5 μm) but also strongly shaped. Raman amplifiers providing flat gain over large bandwidths require multiple pumps at different wavelengths [21] and a careful adjustment of the individual pump powers [22, 23].

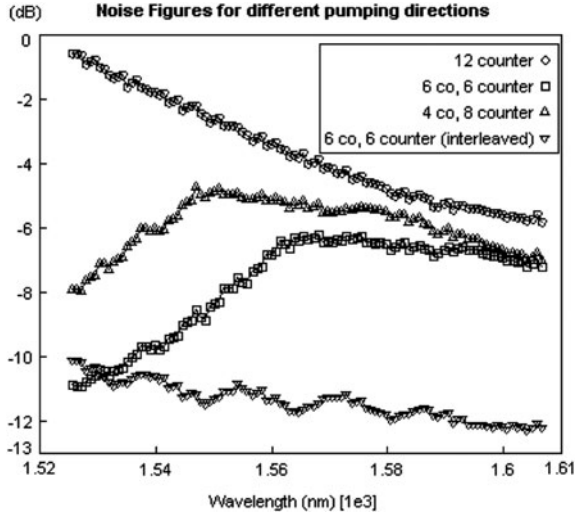
Besides stimulated Raman scattering, spontaneous Raman scattering occurs in the fiber as well producing broadband optical noise that is strongly wavelength- and temperature-dependent. Additionally, double Rayleigh scattering may produce significant amounts of additional noise. The pumping conditions (number and power of co- and counter-propagating pumps) play an important role on the noise characteristics, as shown clearly in Figure 2.4.

Compared with EDFAs compensating fiber loss at the ends of links, Raman amplification is low noise due to its distributed nature. Hence, Raman amplification allows lower launched powers while maintaining the OSNR, which reduces other nonlinear effects in the fiber.

Stimulated Brillouin Scattering

Stimulated Brillouin scattering (SBS) occurs when forward- and backward-propagating lightwaves induce an acoustic wave due to electrostriction with a frequency that equals the frequency difference of the optical waves, and a propagation constant that equals the sum of the propagation constants of the optical waves (phase matching). In other words, the acoustic wave forms a

Fig. 2.4 Effective noise figures for different pumping conditions after optimization of 12 Raman pumps to generate flat gain over 80 nm signal bandwidth after transmission over 100 km NZ-DSF (From Breuer et al. [21], Fig. 9. Reproduced by permission of © 2004 The Institute of Electrical and Electronics Engineers)



traveling index grating, which reflects the incident light wave with a downward Doppler shift. The strength of SBS depends significantly on the type and modulation bandwidth of the transmitted signal. SBS is strongest for narrow-band signals, as a strong coherent grating is produced. It may be detrimental for optical communication systems, as it strongly reflects un-modulated signals and narrow-band pumps. However, the impact of SBS can be effectively lowered by employing techniques that spread the signal power more evenly in frequency (i.e., phase modulation).

2.4.3 Polarization-Dependent Propagation Effects

2.4.3.1 Polarization Mode Dispersion (PMD)

Due to manufacturing imperfections, fibers are not ideally circular and are additionally subject to temperature changes, vibrations, bending, and twisting, which make them birefringent. All of these random mechanisms cause local stress and redefine the local birefringence axes along the fiber length. Hence, light that is propagating along the single-mode fiber is split into two local polarization modes traveling at different velocities. PMD describes this dependence of the propagation velocity of optical signals on the local state of polarization.

At any point along the fiber, light travels as a combination of two polarization eigenstates, which randomly vary with fiber length. For instance, signal power originally sent into one state may partially transfer to the other along the fiber. As a final result, this means that different parts of a signal pulse travel with different velocities causing pulse spreading, which limits the bandwidth of the

transmission system. With this model, PMD at a fixed frequency can be described by two PSPs representing the pair of orthogonal polarization states of slowest and fastest propagation resulting from the integrated polarization characteristics over the whole fiber at that frequency.

The maximum difference between group delays of any polarization state (e.g., the delays of the two PSPs) is defined as the DGD $\Delta\tau$. The *intrinsic* PMD coefficient $D_{\text{PMD},i}$ determines the amount of $\Delta\tau$ per unit length z for very short fiber lengths where birefringence can be assumed to be uniform [24]. Using Taylor series expansion with respect to frequency and considering the first two terms only, $D_{\text{PMD},i}$ is given by

$$D_{\text{PMD},i} = \frac{\Delta\tau}{z} = \frac{d}{d\omega} (\beta_{1,s} - \beta_{1,f}) = \frac{n_s - n_f}{c} + \frac{\omega}{c} \frac{d}{d\omega} (n_s - n_f) \quad (2.19)$$

where $\beta_{1,s}$ is the inverse of the group velocity in the slow PSP, and $\beta_{1,f}$ is the inverse of the group velocity in the fast PSP, where n_s and n_f are the effective refractive index for the slow and fast PSP, respectively. For transmission fiber lengths of interest, however, it cannot be assumed that the orientation and value of birefringence remain constant. The correlation length L_{corr} provides a measure for the strength of the accumulated random change in polarization states. It is defined as the distance where the average power in the orthogonal polarization mode, P_{orth} , is within $1/e^2$ of the power in the starting mode, P_{start} , when omitting the effect of attenuation [25]

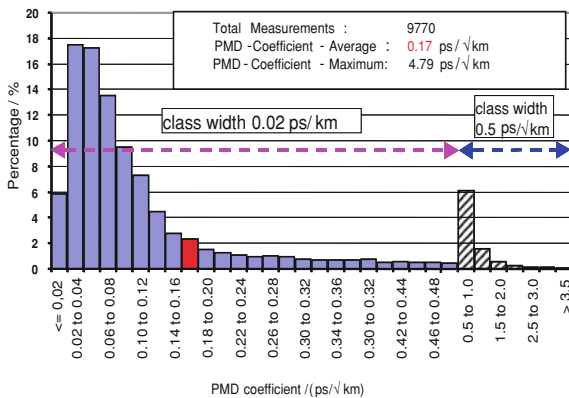
$$|\langle P_{\text{start}}(L_{\text{corr}}) \rangle - \langle P_{\text{orth}}(L_{\text{corr}}) \rangle| = \frac{P_{\text{total}}}{e^2} \quad (2.20)$$

For typical transmission fibers, L_{corr} is only several meters. Here, the randomly and continuously varying DGD over z represents the characteristics for a random walk problem [26], and thus, scales with the square root of z (each incremental *section* may add or subtract to the effects of previous *sections*). In consequence, the PMD coefficient of transmission fibers D_{PMD} determines the amount of average DGD per \sqrt{z} [25]. The stochastic process of varying birefringence can be evaluated analytically with the result that $\Delta\tau$ follows a Maxwellian probability density function (PDF) [27]. The Maxwellian PDF originates from the quadratic addition of three Gaussian processes following an analogy with the statistical model of Brownian motion [28]. It can be used to describe the random distribution of the DGD for fiber distances that are much larger than L_{corr} as follows:

$$P(\Delta\tau) = \frac{\pi}{16} \frac{\Delta\tau^2}{\langle \Delta\tau \rangle^3} e^{-\frac{4}{\pi} \Delta\tau^2 / \langle \Delta\tau \rangle^2} \quad (2.21)$$

Note that $D_{\text{PMD},i}$ is not only time-dependent due to the drift of the environmental parameters but shows also a frequency dependence, which is indicated by the second term in Eq. 2.19. Using the Poincare Sphere as representation of light polarization [29] the PMD vector is, by definition, a Stokes vector pointing in the direction of the slow PSP with a length equal to the DGD [26].

Fig. 2.5 Histogram of PMD coefficient for 9,770 evaluated fibers inside the network of Deutsche Telekom. Dark column represents PMD coefficient average. (From Freund et al. [31], Fig. 12, left. Reproduced by permission of © 2004 The Institute of Electrical and Electronics Engineers)



The frequency dependence of PMD can be described by introducing terms that represent the n -th order dependencies of the PMD vector on frequency. Ignoring third and higher order effects, second order PMD alone consists of two orthogonal components in the frequency domain: polarization chromatic dispersion (PCD) resulting from the linear frequency dependence of the DGD and pointing in the same direction as the PMD vector, and depolarization resulting from the linear frequency dependence of the PSPs and pointing in the orthogonal direction to the PMD vector [24, 30].

The main difference between PMD and the other fiber propagation effects is that PMD shows a strong statistical behavior that is frequency dependent, changes randomly with time, and from fiber to fiber [28, 30]. Hence, it is very time-consuming to measure the influence of PMD on implemented systems and design countermeasures. Further on, terrestrial transmission networks using fiber infrastructure that has been deployed over several years using different generations of fiber might contain fiber cascades with strongly varying PMD coefficients causing many difficulties for implementing high-speed transmission systems (see Freund et al. [31]). Figure 2.5 shows the histogram of PMD coefficients for 9,770 fibers in a Deutsche Telekom network showing the varying degrees of PMD coefficients.

2.4.3.2 Polarization-Dependent Loss/Gain (PDL/PDG)

PDL/PDG (in dB) describes the difference between the maximum and minimum loss/gain with respect to all possible states of polarization. As the polarization is randomly varying along the transmission fiber due to birefringence, fiber PDL gives a statistical value that only accounts for the maximum difference in accumulated loss that any two states of polarization at the fiber output will experience:

$$\text{PDL}_{\text{dB}} = 10 \log_{10} \left(\frac{P_{\text{max}}}{P_{\text{min}}} \right) \quad (2.22)$$

with P_{\max} and P_{\min} being the measured output powers. Note that those two states of polarization always represent orthogonal polarizations [32].

Although the PDL of modern transmission fibers is rather small, and mostly negligible, the PDL of individual components or discrete events along the transmission line (such as couplers, splices, filters) can cause significant power fluctuations with respect to polarization. Furthermore, optical amplifiers such as Erbium-doped fiber amplifiers (EDFA), semiconductor optical amplifiers (SOA) and fiber Raman amplifiers (FRA) or distributed Raman amplifiers (DRA) as commonly referred to may provide unequal gain for all states of polarization, an effect referred to as PDG. The definition for PDG is similar to that of PDL in Eq. 2.22.

Generally, the PDL (or PDG) of concatenated components cannot be determined by just adding the PDL of the individual components as the state of polarization of each PDL-element is different due to the random birefringence of the fiber links connecting these individual components. Consequently, this approximation would give a far too pessimistic number (as it assumes all PDL elements are polarization aligned). A statistical modeling approach is more appropriate in order to estimate the average PDL value and its variation for a given link. It has been found that for a link with many individual PDL elements, the PDF of the overall PDL at the output of that link can be approximated well by a Maxwellian distribution [33]. Additionally, attention needs to be paid to the fact that in combination with PMD, PDL (and PDG) can produce significant amounts of signal distortions, and thus, limit the system reach (see for instance [34–37]).

2.4.3.3 Polarization-Dependent Kerr

Fiber Kerr nonlinearities—resulting in inter-channel (SPM, XPM, FWM) and intra-channel (I-XPM, I-FWM) propagation effects—are actually polarization-dependent. For example, XPM causes nonlinear polarization rotation of the Stokes vector of the propagating channels as shown in Wang and Menyuk [38]. The knowledge of the polarization dependence of Kerr nonlinearities can also be used favorably in transmission system design (see for example [39, 40]). Figure 2.6 shows two eye diagrams demonstrating an effective technique for suppressing intra-channel nonlinear distortions by sending adjacent bits in alternate polarizations. Here, results are shown for a 40 Gbit/s NRZ signal after transmission over a 2,500 km dispersion-compensated fiber link. Clearly, the case using alternate polarization (see Fig. 2.6a) shows much less inter-symbol degradations (here mainly due to I-XPM) compared to the case using standard NRZ modulation (see Fig. 2.6b). Similarly, adjacent WDM channels are often launched in orthogonal polarizations to reduce inter-channel nonlinear interactions between them.

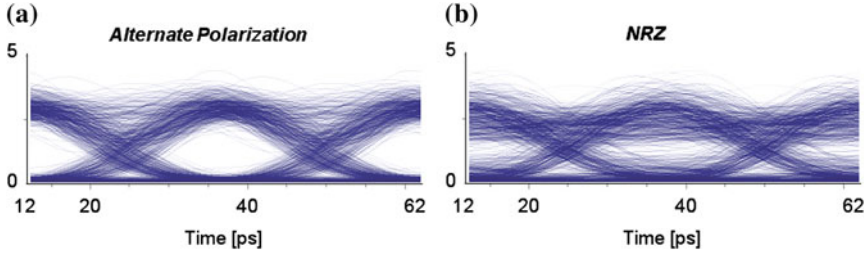


Fig. 2.6 Effective technique for suppressing intra-channel nonlinear distortions: eye diagrams of a transmitted 40 Gbit/s signal when: **a** applying alternate polarizations to adjacent bits; **b** using the standard NRZ format

2.4.4 Modeling Signal Propagation Over Single-Mode Fiber

Figure 2.7 presents a classification of modern modeling techniques for optical fiber [41]. The simplest approach is based on a linear fiber model and includes attenuation and CD effects. This approach is easy to implement and very fast as the whole fiber length can be integrated in one step. However, this approach may only be applicable for systems with very low bitrate, where the signal power does not need to be large due to the small signal bandwidth, and correspondingly, the noise power will be low within such bandwidths. In consequence, nonlinear propagation effects are negligible. Furthermore, it can be used for system designs where nonlinear effects cannot be disregarded to determine a lower bound on system performance.

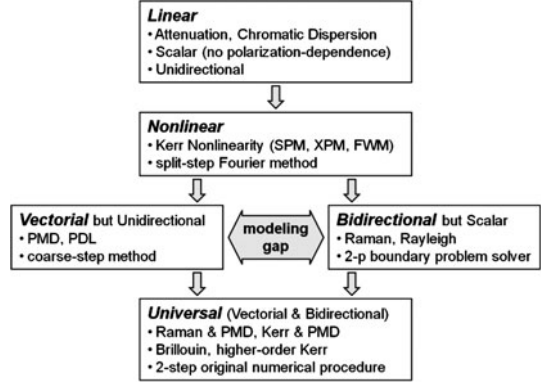
2.4.4.1 Unidirectional Transmission and Scalar Field Description

With an increase of bitrate, the signal power has to be increased as well to maintain an acceptable optical signal to noise ratio (OSNR). At these powers, Kerr nonlinearities of the fiber have to be considered. As a result, signal propagation can be described by the generalized nonlinear Schrödinger (GNLS) equation containing terms responsible for linear and Kerr nonlinear propagation effects (see for instance [9, 25]). This leads to the following representation:

$$j \frac{\partial}{\partial z} A(z, t) + \sum_{k=1}^{\infty} (-1)^{k-1} \frac{j^k}{k!} \beta_k \frac{\partial^k}{\partial t^k} A(z, t) + j \frac{\alpha}{2} A(z, t) = \gamma |A(z, t)|^2 A(z, t) \quad (2.23)$$

where $A(z, t)$ is the complex field envelope of $E(z, t)$, with $E(z, t) = A(z, t)e^{j(\omega_0 t - \beta_0 z)}$, ω_0 being the reference frequency and β_0 the reference phase offset. The GNLS cannot be solved analytically for the general case of arbitrarily shaped pulses propagating over the fiber. However, powerful numerical procedures have been developed with

Fig. 2.7 Evolution of Single-Mode Fiber modeling



the most prominent one being the split-step method. This method is based on the assumption that linear and nonlinear propagation effects can be considered independently over a short fiber distance Δz called split step-size so that:

$$A(z + \Delta z) = [A(z)e^{\Delta z \underline{N}}]e^{\Delta z \underline{D}} \quad (2.24)$$

where \underline{D} is the linear operator accounting for fiber dispersion and attenuation and \underline{N} the nonlinear operator accounting for the Kerr nonlinearity.

If Δz , the so-called split-step size, becomes too large the condition for separable calculation of \underline{D} and \underline{N} breaks down, and the algorithm fails. Hence, careful determination of the optimum split-step size is critical in order to use minimal computational effort for a given accuracy. Typically Δz is adjusted adaptively, an example of which is shown below:

$$\Delta z = \min(\Delta \varphi_{NL} L_{NL}, \Delta z_{\max}) \quad (2.25)$$

where $\Delta \varphi_{NL}$ is the maximum acceptable phase shift due to the nonlinear operator, Δz_{\max} is a maximum split-step size which is set to limit spurious FWM tones [42] and to avoid underestimation of XPM effects due to dispersion induced walk-off. A simple and widely applicable method for determining the minimum Δz_{\max} is given in Rasmussen [43].

While the nonlinear operator \underline{N} is favorably solved in the time domain, the linear operator \underline{D} can efficiently be solved in the spectral domain (using split-step Fourier method, SSFM) or in the time-domain as well (using time-domain split-step method, TSSM). Using SSFM, the Fast Fourier Transform (FFT) can be used for converting data between time and frequency domain [13]. As the speed of the FFT is proportional to $N \log_2(N)$, where N is the number of signal samples in the time or frequency domain, careful determination of the simulation bandwidth and the simulated time duration is important for minimizing the computational effort for given accuracy constraints. Although the SSFM has proven to be the most robust technique [25], both approaches have advantages and disadvantages which depend on the field of application [44].

For small simulation bandwidths and systems with low amounts of accumulated dispersions a TSSM that uses infinite impulse response (IIR) calculations to solve \underline{D} is more efficient than the SSFM (see Fig. 2.4 in Carena et al. [45]) considering some modeling approximations. Generally, this applies also to other TSSM using, for instance, overlap-and-add (OAA) to solve \underline{D} [46]. The main advantage of TSSMs in an environment with an aperiodic representation of the time domain is that the data sequence can be divided easily into small blocks which are handled sequentially. However, the Singleton method [47] can be applied in an SSFM to divide the size of Fourier Transforms into smaller blocks as well. Doing this, simulation speed can be increased by parallelizing the computation effort in both cases. The walk-off between channels in a WDM system becomes significant for higher amounts of accumulated CD and a large simulation bandwidth, and thus, a relatively long bit sequence must be chosen for system performance analysis when using time-domain approaches with aperiodic representations. One further problem is associated with the buildup time of IIR filters or virtual signal delays in case of OAA methods. Simulation data generated during such buildup time must be removed before the system performance is estimated.

These problems do not exist in the case of the SSFM. Here, the problem with different group velocities is eradicated because of the periodic time-domain representation of signals. For example, channels that are delayed in the simulation will be ‘wrapped-around’ to the beginning of the data block: no energy is lost, and the wrap-around represents exactly the data delayed from earlier in the actual data sequence. Note that this artificial periodicity may affect the measured signal statistics, so one should carefully check potential correlations and select the simulated time duration to be long enough. Furthermore, the frequency-dependent phase shift caused by CD is exactly represented using SSFM, not only approximated by a truncated filter impulse response when using TSSM. In time domain, this can be understood as wrapping around an infinite impulse response within the periodic block of samples. This is accurate over all frequencies, whereas TSSM introduces inaccuracies close to the edges of the modeled bandwidth due to truncation effects (Gibb’s phenomenon as shown in Oppenheim and Schaffer [13]). SSFM also shows advantages when modeling dispersion-limited optical systems with vanishing nonlinearity. Here only a single step (equal to the total fiber length) is required. This greatly accelerates computation effort compared to time-domain techniques for solving the linear operator \underline{D} . Finally, the flexibility is a very important issue that should be taken into account when choosing the simulation domain. For example, it is much more difficult to include a realistic dispersion dependency on frequency or the Raman response function into the TSSM than to the SSFM. Any changes of the equations adding higher order derivatives would usually lead to a major rework of time-domain algorithms.

To make simulations of wideband systems even more effective, the SSFM can be extended for the GNLS to accept PS and NBs, and to allow individual sampling of spectrally non-overlapping signals. This approach is often referred to as frequency decomposition (FD) method or mean-field approach [48] and can be used as the main tool for multi-band WDM system simulations at moderate bitrates.

2.4.4.2 Unidirectional Transmission and Vectorial Field Description

An increase of the channel bitrate to more than 10 Gbit/s makes degradations due to PMD noticeable. Modeling PMD in the fiber requires a vectorial approach, describing the electrical field of the propagating light by its Jones vector, and not only by the SOP-averaged electrical field components. To simulate system degradations due to PMD is time-consuming, as PMD is a random phenomenon that is varying in time and frequency. Special statistical treatments such as the coarse-step model [49, 50] (possibly combined with the importance sampling technique [51]) can be applied to avoid an inefficient straightforward integration with very short steps accounting for the short scale length of PMD. Using these techniques, simulations of specific fiber conditions become possible in reasonable time. However, many of those simulation runs are still required to determine statistical information about polarization-dependent fiber characteristics.

Besides statistical modeling of all orders of PMD, the fiber model shall consider Kerr nonlinearities and CD as well as their interplay, especially when investigating high-speed transmission systems. For this purpose, a set of modified GNLS equations (similar to Eq. 2.23) for the two orthogonal polarization components of the electrical field $E(z, t)_{x,y}$ can be used to describe propagation mechanisms over birefringent optical fibers [52]. Assuming rapidly varying birefringence and that the polarization states of light average over the whole Poincare sphere, the Manakov equation has been derived from that [49], with the coarse-step method being introduced as an efficient numerical method for solving it. Later work then led to the Manakov-PMD equation [27, 50], which provides a closed-form and numerically efficiently solvable description of the interplay between CD, Kerr, and PMD effects in optical fiber.

The widely used intuitive coarse-step model, introduced by Wai et al. [49] without strict mathematical reasoning, is based on the assumption that although birefringence perturbations vary from position to position along the fiber length, their impact can be modeled by a concatenation of ‘coarse’ fiber sections, each longer than the correlation length L_{corr} of the fiber, with randomly rotated PSPs and step-wise constant birefringence values. For each of these fiber sections the SSFM, or alternatively, TSSM is used to numerically solve the propagation equations. The length of each polarization section should be much shorter than the total fiber distance in order to model a sufficient number of randomly oriented sections. Studies such as Wai and Menyuk [27], Marcuse et al. [50] showed the validity of the coarse-step model when applied with the correct weighting factors and scattering operations between sections for approximating solutions of the polarization-coupled GNLS equations with the precondition that L_{corr} and L_b (describing the beat length as a measure of fiber birefringence as in Kaminow and Li [24]) are much shorter than L_{NL} . This restriction ensures that the effect of fiber nonlinearity is averaged over the quick oscillation of the signal state of polarization for each polarization section. Consequently, this precondition imposes limitations on the highest possible signal intensity that can be simulated with this method. However, for typical signals used in telecommunications this condition is well satisfied.

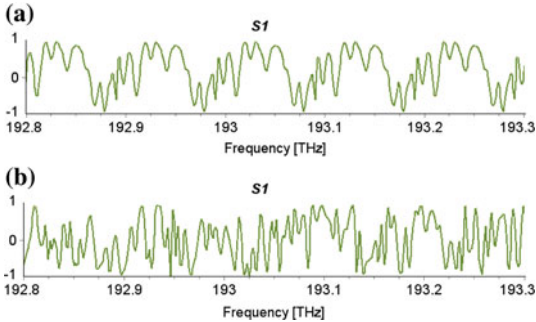


Fig. 2.8 The intrinsic frequency periodicity of the modeled polarization characteristics using the coarse-step model; **a** the above is demonstrated for the first component of the Stokes vector S_1 . The above can be avoided by choosing polarization sections with random lengths; **b** suppression of frequency periodicity for 10% width deviation of the modeled steps

Table 2.1 Accuracy (Δ in % of PDF modeling for different number of Monte-Carlo simulations

	Number of trials		
	$10^3(\%)$	$10^4(\%)$	$10^5(\%)$
DGD	6.2	1.9	0.7
$ \text{PMD}_2 $	13.5	4.4	1.3
PCD	5.8	1.7	0.6
Depol	13.2	4.1	1.3

The individual section lengths should be randomly selected from a Gaussian distribution to avoid a short frequency periodicity of the modeled PMD as described in Fig. 2.8. Figure 2.8a shows the first component of the Stokes vector, S_1 , as a function of frequency for the case that all polarization sections have the same length, whereas Fig. 2.8b shows S_1 when choosing random section lengths (Gaussian with 10% standard deviation). In order to reproduce interesting (e.g., worst case) constellations, it is helpful to be able to store and retrieve the seeding for the random polarization scatterers between sections.

When deploying a statistical model (such as the coarse-step model described above) for emulating the random nature of PMD, it is important to use a sample set that is large enough in order to represent the underlying probability density functions correctly.

Table 2.1 shows results of a study on the modeling accuracy for the PDF of the DGD and second order PMD terms such as its absolute value— $|\text{PMD}_2|$, PCD, and Depolarization. The coarse-step model without any special statistical methods such as importance sampling [51] has been used. A figure of merit Δ is chosen that is defined as the maximum absolute difference between the results from Monte-Carlo simulations (using 100 polarization sections) and analytical predictions as in Nelson and Jopson [53] for an infinite number of polarization sections.

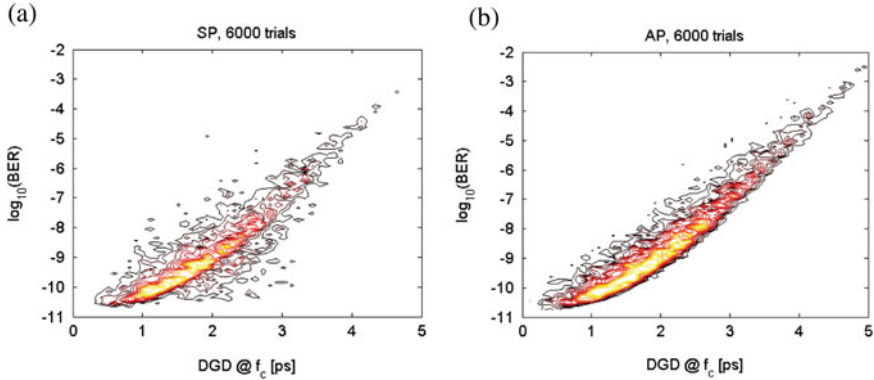


Fig. 2.9 BER versus DGD for: **a** single polarization; **b** alternate polarization. In both cases the system consists of four, 40 Gbit/s OTDM channels propagating over a noisy link with an accumulated mean DGD of 2.1 ps. (From Richter et al. [57], Fig. 4. Reproduced by permission of © 2005 The Institute of Electrical and Electronics Engineers)

Table 2.1 suggests that: (a) when increasing the number of trials by a factor of 10, the accuracy increases approximately by a factor of $\sqrt{10}$, and (b) the modeling accuracy of the PDFs of Depolarization and $|PMD_2|$ is approximately half as good as that for the PDFs of DGD and PCD using the same number of trials.

To assess the simulation accuracy of the spectral PMD modeling, the auto correlation functions with respect to frequency for the PMD vector and for DGD should be evaluated. For a given product, P , of average root-mean-squared DGD $\langle\Delta\tau_{\text{rms}}\rangle$, and measurement bandwidth B_m , as defined in Shtaif and Mecozzi [54] the simulation accuracy Δ can be calculated by comparing Monte-Carlo simulations with theoretical considerations. For example, an accuracy of $\Delta < 2\%$ can be achieved for $P = \langle\Delta\tau_{\text{rms}}\rangle B_m = 100$ using averaged results from 50 Monte-Carlo simulations. Note that increasing the number of simulation trials does not improve the modeling accuracy.

As an application example, the statistical signal performance for 4*40 Gbit/s OTDM transmission over 520 km dispersion-compensated SSF with an accumulated average DGD of 2.1 ps is modeled using the method described in Richter et al. [55]. Figure 2.9 shows contour plots of bit error rate (BER) versus DGD for the 40 Gbit/s tributaries from 6,000 simulation trials with random PMD realizations using a deterministic BER estimation method accounting for arbitrary signal statistics and polarization states of optical noise and signal in front of the receiver [56]. Figure 2.9a shows results for the case that all pulses are transmitted with equal polarization, while Fig. 2.9b depicts results for the case that the 40 Gbit/s tributaries are launched in alternate polarizations.

The use of “link emulators” to investigate the impact of combined CD–PMD and PDL effects is another possible approach for modeling the transmission link. With such emulators DGD, and the second order PMD characteristics—PCD and depolarization—can be set individually and specific combinations of first and

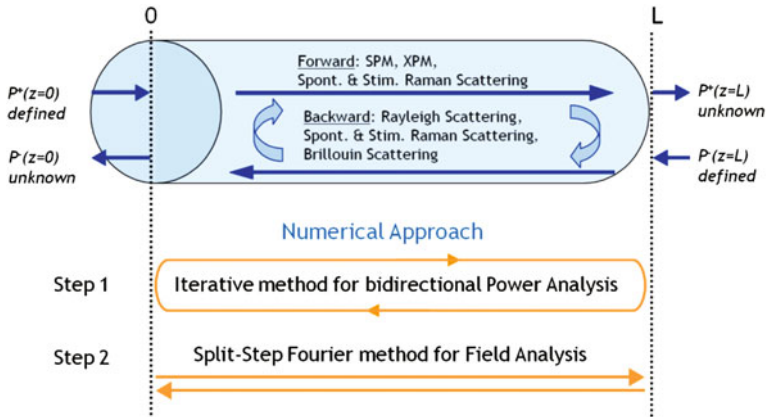


Fig. 2.10 Bidirectional signal propagation in fiber and two-point boundary problem, [63, section *UniversalFiber*] (Copyright 2011 VPIsystems. Used by permission of VPIsystems Inc)

second order PMD can be selected. Many other possible implementations have been proposed as in Francia et al. [58], Kogelnik et al. [59], Eyal et al. [60], Orlandini and Vincetti [61] which typically differ in the amount of residual third and higher order PMD terms that cannot be controlled by the emulator.

2.4.4.3 Bidirectional Transmission and Scalar Field Description

The utilization of Raman amplifiers and the increase in bitrates have raised the need for further development of fiber modeling techniques. Raman amplification requires bidirectional fiber modeling, as the pumps and signals propagate in opposite directions in many configurations of interest. Noise from spontaneous Raman scattering is always generated in both directions as well. To model bidirectional signal propagations in fibers, at least a two-point boundary value problem has to be solved taking into account the initial conditions at both fiber ends. In case of reflective and/or lossy splices (or other discrete scattering events) located along the fiber the complexity is raised to a multipoint boundary value problem. This type of problem is impossible to solve using ordinary unidirectional numerical integration methods without neglecting interactions between counter-propagating waves. To take into account bidirectional interactions an original numerical procedure consisting of two stages can be applied as presented in Fig. 2.10 and further described in Poloyko et al. [62], Photonic Modules Reference Manual [63].

In the first stage, a bidirectional power analysis is performed and so the complex amplitudes of the sampled signals at the input fiber ports are replaced by the corresponding parameterized (time-averaged power) representation. This step excludes time-dependent effects from the analysis and reduces the problem to a

two-point boundary value problem for ordinary differential equations describing the signal power propagation along the fiber. The corresponding two-point boundary value problem can effectively be solved by an iterative algorithm. Simulation accuracy and speed depend strongly on the frequency discretization that is applied for this approximation process. It is useful in practical calculations to specify different resolutions for frequency regions containing sampled data signals and other regions, only containing optical noise.

In the second stage, the optical field analysis can be performed by first substituting the power distributions in both directions along the fiber distance that have been found after completing the first step into the full GNLS equation (see Eq. 2.23). With this substitution, terms including counter-propagating signal powers become defined everywhere along the fiber. This approach is possible assuming that dynamic (time and pulse shape-dependent) propagation effects induced by interactions of counter-propagating waves are negligible. As their interaction time is very short only the spatially resolved average power of counter-propagating signals is of relevance. Furthermore, it can be assumed that FWM between counter-propagating waves is negligible due to the phase mismatch. As a result, the two-point boundary problem reduces to a problem similar to the unidirectional propagation, and the SSFM can be used for effectively solving it. Depending on the specific application, the field analysis performed in the second step could be done for frequency bands propagating in the forward, in the backward, or in both directions.

When modeling bidirectional propagation effects over heterogeneous fiber links consisting of several different fiber spans it is important to consider each span by its individual fiber characteristics (e.g., attenuation, CD, Rayleigh coefficient, nonlinear index, core area, Raman gain etc.) and to add information about losses and reflections at fiber splices and fiber ends.

For an accurate modeling of wideband applications it is important to account for the wavelength-dependence of relevant fiber properties as well. For instance, the Raman gain profile of the fiber needs to be known when modeling SRS. As the Raman gain depends on the pump frequency, either many profiles measured at different pump wavelengths are to be supplied and the actual Raman gain at the frequencies of interest is obtained by interpolation, or Raman gains at different pump wavelengths should be approximated using correct frequency scaling [62, 64].

Even more care is needed when trying to adjust multiple pumps at different wavelengths in order to achieve flat amplification over a wide spectral width. Special optimization algorithms are needed for this task due to the large number of open parameters [65, 66]. To make those optimization algorithms applicable for real-world problems, it is essential that they consider not only all Raman-related propagation effects, but also other power-related effects along the fiber. For instance, signal–signal Raman interactions, Rayleigh and Brillouin scattering, and power-related variations of broadband pump sources can cause significant amplifier degradations [67].

The possibility to model the different physical effects individually or in combination, and to control their strengths is important for the assessment of sources

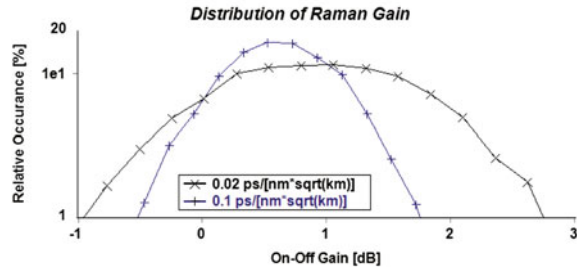
for system degradations (and saving computation time). Further on, adjustment factors could be introduced to scale the strength of nonlinear interactions due to SPM, XPM, and SRS between co-propagating bands. These factors can for instance, account for the dependence of Raman interactions on the mutual polarization of the interacting fields, for example: when using information that was obtained by measuring the Raman gain coefficient for a short (\sim meters) fiber with co-polarized signal and pump, an adjustment factor of 0.5 should be used in order to treat the Raman gain correctly; when simulating long (~ 100 km) fiber spans, the polarizations of pump and signals vary randomly with respect to each other due to the frequency-dependence of PMD. As another example indicates, the SPM effect can be scaled by the factor $8/9$ to account for the averaging of Kerr nonlinearities for applications where PMD and PDL can be neglected, if the value of nonlinear index coefficient n_2 used for the simulations has been measured without considering polarization averaging over long fibers [25]. Similarly, the XPM effect between orthogonally polarized signals propagating in different sampled bands over high-birefringence fiber can be scaled accordingly to account for the fact that XPM is much stronger for signals with aligned polarizations.

2.4.4.4 Bidirectional Transmission and Vectorial Field Description

For many years, the development of bidirectional and vectorial models was independent and went in separate directions, using completely different numerical techniques. However, high bitrate Raman-amplified systems required the consideration and inclusion of both, PMD and bidirectional Raman effects [68]. For this reason vectorial and bidirectional methods have been unified into one universal model as discussed in Photonic Modules Reference Manual [63, section *UniversalFiber*]. An advantage of this unification is that polarization-dependent effects during Raman amplification can be considered. This is for example, useful for cases of polarization-multiplexed systems, not perfectly depolarized pumps, or polarization-sensitive discrete fiber events (such as PDL at splices). Figure 2.11 shows how the Raman gain would be distributed for co-polarized pumping over fibers with different PMD coefficients if a Raman pump is used that is not depolarized. The SRS effect requires signals and pumps to be polarization-aligned, which is on average the case over half the distance in standard transmission fibers. However, depending on the actual polarization states along the fiber the alignment varies. For fibers with low PMD coefficients the statistical variation could be large, which is the reason why depolarized Raman pumps are preferred in scenarios with co-propagated pump(s).

The development of numerical methods for this challenging task makes it possible to take into account a number of additional important propagation effects; for instance, Brillouin backscattering, multiple Rayleigh scattering, and back-reflections/attenuations at fiber splices. The bidirectional vectorial consideration is very complex but represents the most powerful simulation technique that is currently available.

Fig. 2.11 Distributions of Raman gain for fibers with different PMD coefficients using a single co-propagated Raman pump without depolarization. (Note: 0 dB gain corresponds to perfect compensation of fiber loss for the case that a depolarized pump is used)



In summary, the ultimate (universal) model for single-mode fiber propagation supports

- the modeling of wideband bidirectional transmission and interaction of signals, pumps, and noise
- the representation of signals, pumps and noise by sampled waveforms or time-averaged parameters (e.g., to keep them separately and increase simulation efficiency), and
- the wavelength-dependent definition of all fiber parameters (attenuation, CD, effective mode area, nonlinear coefficient, Brillouin and Raman scattering responses, Rayleigh backscattering, birefringence profile, etc.)

The full vector model (Jones) for arbitrary polarization dependencies and the scalar model (SOP averaging) for a linear polarized approximation define the main modes of operation. In scalar mode, the universal model shall include attenuation, CD, Kerr nonlinearities with delayed-response terms, SRS between pumps, signals and noise, point reflections and losses, Raman-induced changes of the nonlinear refractive index, wideband noise generation due to spontaneous Raman scattering at any temperature, stimulated and spontaneous Brillouin scattering including the linewidth-dependence of the reflection coefficient, and multiple Rayleigh scattering. In vectorial mode, the model shall *additionally* be able to account for all-order PMD (with optional techniques to weight statistics and emphasize less likely events), and polarization dependencies of nonlinear Kerr and scattering effects.

Furthermore, it is very helpful to have the ability to switch individual propagation effects on/off and to define heterogeneous fibers consisting of multiple spans of different fiber types that are connected by lossy and reflective splices. Parameters that control the numerical accuracy and calculation speed of underlying algorithms as well as means for visualizing fiber characteristics versus distance or frequency and the numerical convergence of calculation algorithms are also extremely important and helpful.

2.4.4.5 Parametric Analysis

While a high level of detail is important for component and subsystem design, rapid visualization of important performance measures can aid in the overall understanding of systems, and thus, be very useful in system and network design. In conjunction with approximate design rules network engineers can access, without demonstrating

very detailed photonics knowledge, whether a network (or sub-network) is likely to operate properly or not. Such a quick performance assessment can be achieved using a parametric approach that avoids time-consuming simulation runs when verifying complex network configurations and identifying potential design flaws [69].

Figure 2.12 shows a sample network configuration and typical results of the parametric system validation process. Figure 2.12a depicts the simulation setup¹ of a three-node network that consists of two parallel paths connecting N1 and N2 with H2, and a common Raman-amplified 140 km link connecting H2 with N3. A total of 16 C-band channels each carrying 10 Gbit/s are used for communication between N1 and N3, while 16 L-band channels are deployed between N2 and N3. The individual SSMF fiber spans are post-compensated by appropriate DCFs; EDFAs are placed at H1 and H2 accounting for the accumulated loss. Figure 2.12b shows optical signal powers versus topology (left) and versus frequency at N3 (right). Figure 2.12c shows a parametric plot illustrating the relationship between accumulated SPM and CD for two channels (one in C-band and one in L-band) as they propagate through the network. Without the need to run detailed simulations the results depicted in Fig. 2.12 indicate that one Raman pump per band is not sufficient to achieve flat gain and the power in both bands is very unbalanced requiring additional gain adjustments before entering into any possible links that are following. Furthermore, the designer is able to locate places where large amounts of accumulated CD and nonlinear phase shift occur simultaneously, something that can lead to significant penalties. Hence, the example discussed above emphasizes quickly the limitations of the chosen amplification and dispersion maps.

2.5 Optical Amplification

Several technologies for optical amplification have been introduced over the years addressing different system requirements and applications: semiconductor optical amplifiers (SOA), rare earth ion doped fiber (or waveguide) amplifiers (e.g., Erbium-doped fiber amplifier—EDFA), and discrete and distributed fiber Raman amplifiers (FRA). Especially with the invention of the EDFA in the late 1980s the development of fiber-optic communication systems accelerated rapidly [70]. Electro-optic repeaters could be replaced by the more robust, flexible, and cost-efficient EDFAs. The main requirements on EDFA technologies from a systems design perspective are: operation over wide wavelength ranges, high output powers, equal gain to each channel, low-noise characteristics, negligible crosstalk between channels, mechanisms for gain control, high energy efficiency, and low cost.

¹ using VPITransmissionMaker™ Optical Systems, Version 8.6.

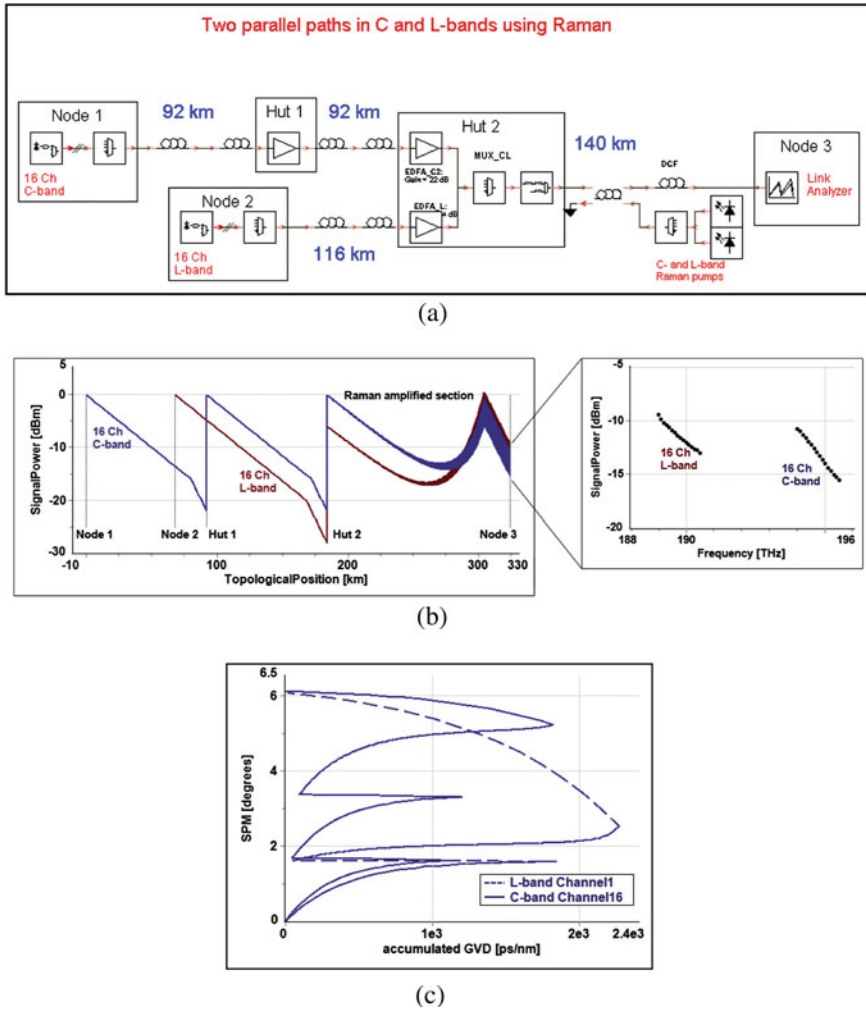


Fig. 2.12 **a** Optical network with two parallel paths, each carrying $16 \times 10\text{Gbit/s}$, with Raman-amplified common link; **b** optical signal powers versus topology and versus frequency; **c** parametric plot illustrating the relationship between accumulated SPM and CD for two channels as they propagate through the network

The requirements of low noise, wide bandwidth, high power, and gain flatness cannot be met with simple EDFA designs employing only a single pump, and a single amplifying fiber. Optical amplifiers operating over multiple wavelength bands with improved performance have incorporated sophisticated technological advances including multi-stage doped-fiber amplifier designs with pump reuse, mid-stage gain equalization, novel dopants and hosts, as well as topological innovations such as bidirectional or parallel amplifiers. Additionally, alternatives such as Raman amplification in non-doped fibers using multiple pump

wavelengths and cascaded pumping have been introduced to increase the amplifiable system bandwidth and required repeater spacing.

Obviously there are many combinations of amplifier topology, fiber, pump and passive component technology that could produce a cost-effective, low-noise, wide-bandwidth, high-power, spectrally flat, and power-efficient amplifier. A detailed discussion on the theory and design of EDFAs is given in Desurvire [71], Becker et al. [72]. In what follows we present the main theoretical concepts and underlying fundamental operating principles for these devices that are intended to facilitate their modeling. In Chap. 3 a “black-box” approach for their modeling is also presented.

2.5.1 EDFA Theory

A single-mode Er-doped fiber can be modeled using the rate and propagation equations for a three-level laser medium or using the equations for a simplified two-level laser medium [73]. Figure 2.13 shows the energy diagram of Erbium ions in glass hosts. For 980 nm pumping, carriers are absorbed from the ground level to the third laser level. Due to phonon relaxation (in the times scale of μs) carriers transit down to the second level almost immediately where they reside with an average lifetime of approximately 10 ms and distribute due to thermalization processes. The same effect could be achieved for 1,480 nm pumping, causing absorption of carriers from the ground level directly to the second laser level. With this, and ignoring other, higher order effects in the Er-doped fiber such as excited state absorption, up-conversion, spectral-hole burning, and others, it is a reasonable assumption to model the gain and noise behavior in an EDFA using only a two-level laser medium. The third level comes into play only via the coefficients of absorption from the ground level. Note that the two-level model is applicable for silica host glasses, but not for glasses where the third level has a comparatively long lifetime (e.g. fluoride). From the above it is clear that a three-level scheme must be used.

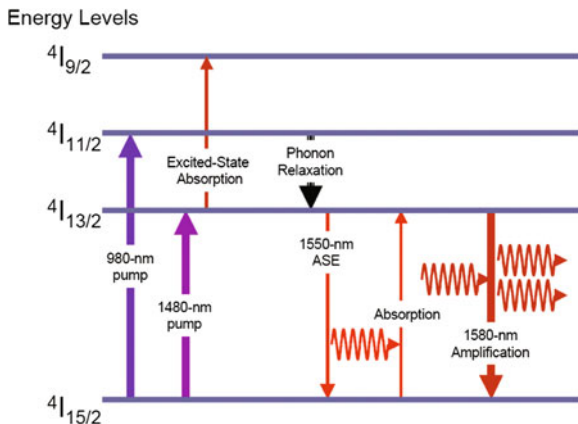
2.5.1.1 Gain

The gain in EDFAs is strongly dependent on the carrier inversion, or in other words, the amount of carrier population in the upper state compared to the total number of carriers. It is determined by the pumping scheme, and is influenced by the existence of co-dopants such as germanium and alumina. The wavelength dependence of local gain can be written as presented in Desurvire [71]:

$$g(\lambda) = [N_2\sigma_e(\lambda) - N_1\sigma_a(\lambda)]\Gamma(\lambda) \quad (2.26)$$

where N_2 , and N_1 denote the carrier populations of the upper and lower states respectively, σ_a , and σ_e denote the absorption and emission cross-sections respectively, and $\Gamma(\lambda)$ is the overlap factor, i.e., the area of overlap between

Fig. 2.13 Transitions between energy levels in an EDFA as presented in User's Manual [74, pp. 12] (Copyright 2011 VPIsystems. Used by permission of VPIsystems Inc)



Erbium ions and the optical signal mode in the doped fiber. Note that the population inversion shows a strong local dependence so gain may differ over the length of the doped fiber.

Figure 2.14 shows simulation results characterizing the performance of a single stage EDFA for different pumping schemes. Figure 2.14a shows amplifier gain as a function of population inversion around the 980 nm (pump) wavelength. Perfect inversion is possible as the emission cross-section is zero at 980 nm. This results in small noise generation for 980 nm pumped EDFA configurations. Figure 2.14b shows gain as a function of population inversion at 1,480 nm (pump) and around 1,550 nm (C-band). For the depicted inversion profile, the transparency point ($g = 0$ dB/m) for 1,480 nm pumping is at about 75% population inversion. So, perfect inversion is not possible, which results in increased noise generation. The figure depicts the strong wavelength dependence of the gain, which results from the wavelength dependence of population inversion.

Ignoring noise to begin with, the average signal power dependence on doped fiber length is given by

$$\frac{dP}{dz} = g(\lambda, P)P \quad (2.27)$$

For small signal powers, the total amplifier gain is usually independent of the incoming power. If the power launched into the doped fiber is increased over a certain level, stimulated recombination starts to affect carrier population inversion. Every photon created by stimulated emission transfers one ion from the upper state to the lower state. This results in gain reduction until absorption of pump power and stimulated plus spontaneous emissions are balancing each other. This effect is known as gain saturation. The saturation characteristic of an EDFA is very complex, as it is dependent on fiber distance. Assuming a homogeneous power distribution along the EDFA, the ratio of input power P_{in} and saturation power P_{sat} is given by Iannone et al. [25]

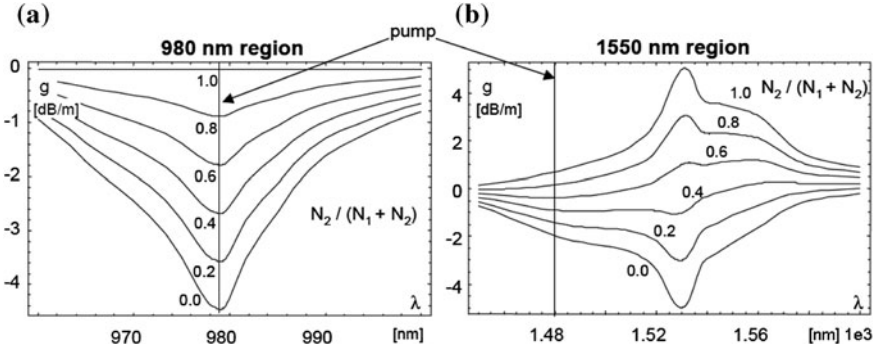


Fig. 2.14 Sample gain/loss profile for various values of population inversion in a typical EDFA. (From Richter [20]. Reproduced by permission of the author © 2002, Andre Richter)

$$\frac{P_{in}}{P_{sat}} = \frac{1}{\log_e(4)} \frac{G_0 - 2}{G - 1} \log_e \left(\frac{G_0}{G} \right) \quad (2.28)$$

where G is the amplifier gain with $G = P_{out}/P_{in}$. In the above G_0 is the small-signal (or linear) amplifier gain, and P_{sat} is defined as the input power where $G/G_0 = 0.5$.

2.5.1.2 Noise

Spontaneous transitions of photons from the upper state to the ground state accumulate along the doped fiber and stimulate other transitions which cause self-amplification, or amplified spontaneous emission (ASE). ASE noise is un-polarized and builds up in the forward and backward directions. The amount of ASE noise created at each end of the doped fiber depends on the local population inversion. For system-level applications ASE noise is well approximated by a Gaussian random process [71, 75]. Its PSD at the amplifier output can be written as:

$$S_{ASE} = \frac{P_{ASE}}{B_m} = 2n_{sp}(G - 1)hf, \quad \frac{1}{n_{sp}} = 1 - \frac{N_1\sigma_a(\lambda)}{N_2\sigma_e(\lambda)} \quad (2.29)$$

where n_{sp} is the spontaneous emission factor, G is the total amplifier gain, hf is the photon energy, and P_{ASE} is the ASE noise power measured over a bandwidth of B_m . As the ASE noise power is proportional to the gain and n_{sp} it can be minimized by operating the EDFA at high population inversion.

The noise performance of amplifiers is usually characterized by the noise figure (NF) being defined as the degradation of the electrical signal-to-noise ratio (SNR) due to the amplifier and measured with an ideal photodetector. From Derrickson [32] the definition for the noise figure is formulated as:

$$NF = \frac{\text{SNR}_{\text{in}}}{\text{SNR}_{\text{out}}} \approx 2n_{\text{sp}} \frac{G-1}{G} + \frac{1}{G} \quad (2.30)$$

where it is assumed that the ASE–ASE beat noise component can be neglected [76]. With this, the noise PSD can be written as a function of the NF and the gain:

$$S_{\text{ASE}} \approx (NF G - 1) h f \quad (2.31)$$

where both values (NF and gain) are being calculated without knowledge of the internal architecture of the optical amplifier. Practical EDFA designs consist typically of multiple stages where the first stage operates as a low-noise pre-amplifier, preferably pumped at 980 nm to ensure small NF . This is advantageous as according to the chain rule, the noise figure of an amplifier cascade is mainly determined by the NF of the first amplifier in the chain [77]. The following stages operate as a power amplifier, preferably pumped at 1,480 nm as this concept provides higher power conversion efficiency. Isolators being placed between stages prevent saturation of the previous stages due to backward propagating ASE noise from the following stage. Also, filters are used to suppress ASE noise outside the signal bandwidth and perform gain equalization.

2.5.1.3 Optical Signal-To-Noise Ratio

One important performance parameter is the optical signal-to-noise-ratio (OSNR) which is defined as the ratio of optical signal power and optical noise power within a measurement bandwidth B_m . Using Eq. 2.31 above we can derive the following:

$$\text{OSNR} = \frac{P_{\text{out}}}{S_{\text{ASE}} B_m} \approx \frac{P_{\text{in}}}{(NF - 1/G) h f B_m}, \quad P_{\text{out}} = G P_{\text{in}} \quad (2.32)$$

The OSNR can be directly related to system performance for applications that are limited by optical noise. For a signal with perfect extinction ratio, assuming that signal-ASE beat noise and ASE–ASE beat noise dominate the electrical noise (e.g., ignoring thermal and shot noise added by a direct-detection optical receiver) and further assuming that no other propagation effects, such as for example CD, Kerr, and others, deteriorate the eye opening, the Q factor can be easily related to the OSNR at the input of the optical receiver [24] as follows:

$$Q = 2 \text{ OSNR} \frac{\sqrt{B_o/B_e}}{1 + \sqrt{1 + 4 \text{ OSNR}}} \quad (2.33)$$

In the above, B_e is the electrical bandwidth of the receiver and B_o is the bandwidth of the optical filter in front of the receiver. For $B_m \neq B_o$, the OSNR value should be scaled by the factor B_o/B_m before being used in the Q factor

calculation. In most applications, the bandwidth of optical noise sources is much wider than the signal rate, and thus it can be assumed that the OSNR is proportional to the signal rate if optical filtering effects are neglected. So when increasing the signal rate for instance from 10 Gbit/s to 40 Gbit/s using the same modulation format and filter bandwidths that are proportional to the signal rate, the OSNR requirement rises approximately by 6 dB.

2.5.2 *Systems Modeling and Performance*

2.5.2.1 **Black-Box Modeling**

A phenomenological modeling approach that requires parameters describing the behavior of EDFAs in a system context is better suited for the simulation of a WDM transmission line since the internal architecture and parameters of the amplifiers are typically not known at this level of design. For this purpose Black-Box modeling is favorable. The approach to consider amplifier gain and noise figure as fixed functions of wavelength is an approximate one since it ignores for instance dependencies of pump and signal powers on the EDFA gain and noise characteristics, yet for many system simulation applications it is fairly adequate.

More accurately, but still making a number of simplifying assumptions on the physics in the doped fiber, the spectral gain and noise behavior of the EDFA can be calculated requiring no detailed knowledge of the internal amplifier details (e.g., emission and absorption characteristics, dopant density, reflection properties) [78–82]. As a consequence of the assumption that the doped fiber saturates homogeneously, the gain characteristics (with respect to wavelength, mode of operation, possibly pump power) can be calculated from a number of data files obtained from standard optical spectrum analyzer measurements performed on an actual physical device [32] or from detailed component-level simulations of architecturally complex doped amplifier designs [83]. The noise behavior is typically estimated in a similar manner by interpolating data taken at different points of operation, even though a solid physical background for this approach does not exist. Black-box modeling is computationally fast and therefore more efficient for use in system-level simulations and provides possibilities for incorporating internal automatic gain or power control as well.

If not compensated carefully, when designing high-capacity WDM systems utilizing a cascade of EDFAs, the individual gain and noise characteristics of each EDFA may result in significant fluctuations of signal power and OSNR between WDM channels. Figure 2.15 shows results of a related case study. The optical signal powers and OSNR values of 32 WDM channels in the C-Band are plotted versus propagation distance. The WDM band has been propagated over ten 80 km dispersion compensated fiber spans with the loss of each span being compensated by an EDFA. All amplifiers are set to provide the same average gain and have the

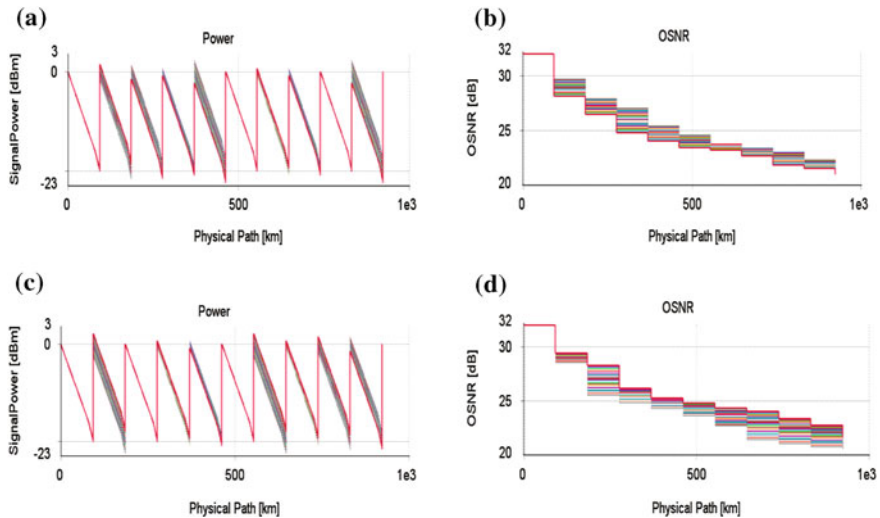


Fig. 2.15 Signal Power shown in (a) and (c) and OSNR shown in (b) and (d) for 32 channels in C-Band for propagation over cascades of 10 EDFA with different gain and noise tilts. Note that (c) and (d) present an inverted order of EDFAs compared to (a) and (b)

same average noise figure, however, they have varying gains and noise tilts. The upper graphs (Fig. 2.15a, b) are obtained using an arbitrary order of EDFAs; the lower graphs (Fig. 2.15c, d) are obtained using the inverted order of amplifiers. Overall, even though the same ten EDFAs are used in both cases, a significant spread in WDM channel signal power and OSNR is obvious in Fig. 2.15a, c for the former and Fig. 2.15b, d for the latter.

2.5.2.2 Power Transients

EDFAs, including their gain stabilization circuits, do not react instantly to abrupt changes in input power which might be caused by events such as automatic network re-configuration, failure of components, or switching of optical packets. The resulting power transients are especially problematic in networks with a complex topology due to numerous feedback mechanisms. Modeling dynamic transmission phenomena in transparent networks differs significantly from modeling stationary processes. Of particular interest is the analysis of dynamic power perturbations that propagate through the optical network and thus change the average power level at components along the optical path and at the receiver (see for example Fig. 2.16b and descriptions thereto further down). In a worst-case scenario, channel switching effects can create chaotic oscillations of signal powers that propagate through the network as described in Yoo et al. [84].

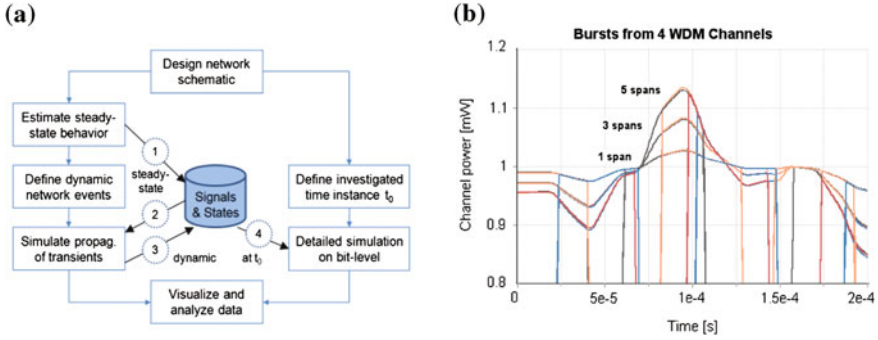


Fig. 2.16 **a** Workflow for emulating dynamic events in optical networks and investigating the resulting performance impacts; **b** Dynamics of random traffic bursts from 4 WDM channels: channel powers after one, three and five amplified spans using gain-clamped EDFAs; (From Richter et al. [85], Figs. 2 and 3. Reproduced by permission of © 2010 The Institute of Electrical and Electronics Engineers)

To emulate the characteristics of dynamic networks, it is necessary to combine investigations on bit-level (ns to sub-ps time scales) with analysis of effects with much larger response times (up to a few ms). The evolution of signals in such applications is often affected by varying noise levels and transient processes in control loops with various characteristic times. Figure 2.16a shows a general workflow for emulating dynamic events in optical networks and analyzing their performance impact [85]. First, slowly varying network events are emulated using parametric signal representations that track information about important signal attributes versus time, frequency, and topology. When starting the network emulation, only changes to these attributes are calculated in the context of a global evolution analysis considering all signal paths. The origin of the limiting effects can be detected by recording and analyzing important link characteristics at pre-defined topology points as described in Richter et al. [69]. With the gathered parametric information, estimates of the system quality can be obtained using functional relationships that are derived from measurements or experience (design rules). For example, Fig. 2.16b shows the growths of power fluctuations of random traffic bursts from four WDM channels after passing one, three, and five amplified spans using gain-clamped EDFAs.

In an optional second step, detailed simulations down to the bit-level can be performed to reveal the physical limitations at a certain, identifiable time instance of the network (e.g., during turn on, stable operation, channel switching, component failure). For this purpose, the time-dynamic information about the network (e.g., signal and equipment state data at discrete time instances) from the first step is used to define initial conditions for a detailed simulation on a bit-level.

2.6 Optical Signal Generation

2.6.1 *Types of Modulation*

The technology of optical transmitters can be divided into two broad categories: transmitters made of a laser that is modulated directly by the electrical driving signal carrying the information sequence called directly modulated laser (DML), and transmitters that are combinations of a laser delivering a continuous wave (CW) followed by an external modulator (called externally modulated laser or EML) or a cascade of such devices.

2.6.1.1 Direct Modulation

The applicability of directly modulated lasers in modern transmission systems is limited due to the narrow modulation bandwidth of lasers and the generation of frequency fluctuations with time (chirp) that are hard to control or eliminate. Chirp combined with CD critically affects the channel transmission performance over fiber. Recent work on chirp-managed lasers (CMLs) has proven that high dispersion tolerance could be achieved when using the directly modulated laser in combination with a carefully tailored optical filter applied to counteract the adiabatic chirp from a laser [86].

The behavior of DMLs is most easily predicted using laser rate equation models requiring physical parameters describing the internal cavity mechanisms of the laser. These physical parameters can be easily estimated by fitting theoretical curves to measured data for intensity modulation response, light–current characteristic, and time-resolved chirp [87]. Simple rate equation models ignore the details of the optical spectrum (assuming a single-mode, both in the longitudinal and transverse directions). Specifically, distributed feedback (DFB) lasers are well suited for a description by rate equations because the DFB design allows suppressing side modes efficiently. However, in order to evaluate such suppression and design optimal DFB structures, laser models that include the longitudinal structure of the laser such as the transmission-line laser model and its variants [88, 89] are required. If the variation of the carrier density is represented longitudinally these detailed models can predict chirp due to longitudinal spatial hole burning and even instabilities caused by this effect.

2.6.1.2 External Modulation

WDM transmission systems employing channel bitrates of 10 Gbit/s and higher typically deploy externally modulated transmitters. These provide a high wavelength-stability, small amount of distortions, high extinction ratio, and a defined frequency chirp characteristic that can be controlled to counteract for fiber propagation degradations due to CD and SPM [90]. The laser in an externally

modulated system is operated under CW conditions with a well-defined linewidth and intensity noise. For 10 Gbit/s systems and above the frequency spectrum of the intensity noise and the detailed lineshape may be important. Also, the correlation between the instantaneous frequency and the intensity could be relevant and must be considered (these characteristics can be predicted using rate-equation laser models or even transmission-line laser modeling).

Two types of modulators are commonly used, namely Mach–Zehnder modulators (MZM) and electro-absorption modulators (EAM) [91]. MZMs provide usually a better defined transfer characteristic. They can be designed to have zero frequency chirp, or a chirp that can be controlled by the electrical drive voltage. EAMs are easier to integrate to the device, but come with an intrinsic chirp which is proportional to the gradient of the emitted optical power with respect to applied voltage. They require careful characterization over a wide range of wavelengths, bias, and temperature operating conditions. Furthermore, EAMs have a nonlinear transmission-voltage characteristic and a voltage-dependent chirp characteristic. They can be represented in simulation models by using polynomial fits, or multidimensional lookup tables [92]. More advanced models combine the spectral and dynamic characteristics (e.g., important for wideband applications) and polarization sensitivity, as well as specific electric properties of the driving signal [93]. Figure 2.17 shows static and dynamic characterization and validation results of a typical EAM. Figure 2.17a compares measured and simulated static power transfer functions of the investigated EAM using a single spectral band of about 10 THz to allow a simultaneous modulation of 13 optical carriers between 1,540 and 1,588 nm. Figure 2.17b shows comparisons of measured and simulated normalized dynamic EAM power transfer function and alpha factor characteristics for single channel 40 Gbit/s NRZ modulation.

The Mach–Zehnder modulator is based on the interference principle which is well represented by a few parameters in a physical model. The electric field of the incident optical signal is split to propagate over two branches, over which the field experiences different amounts of phase change due to the electro-optic effect. The optical signals of the two branches are then recombined which results in an interference pattern that is directly related to the phase difference between the two branches. The amount of phase change over each branch is controlled by electrical voltages. With the lumped model approximation the transfer function of the MZM can be written as:

$$\frac{E_{\text{out}}(t)}{E_{\text{in}}(t)} = \cos[\Delta\Phi(t)]e^{-j\alpha \tan(\Delta\Phi_{\text{bias}})\Delta\Phi(t)} \quad (2.34)$$

where $E_{\text{in}}, \text{out}(t)$ is the electric field at the input and output of the modulator respectively, $\Delta\Phi(t)$ is the phase difference of the electric fields in the two branches of the MZM, $\Delta\Phi_{\text{bias}}$ is the bias point of operation, and α is the so-called α -factor defining the chirping behavior of the MZM. This α -factor is further defined as the ratio of the phase change to the intensity change at the output of the MZM [92]:

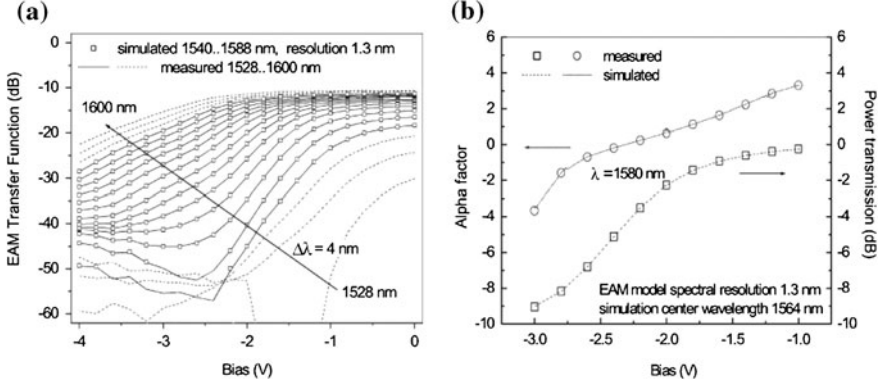


Fig. 2.17 Static and dynamic EAM modeling. **a** measured (lines) and simulated (squares) power transfer function using single ~ 10 THz band to allow a simultaneous modulation of 13 optical carriers in 1,540–1,588 nm; **b** dynamic power transfer function (normalized to 0 dB at 0 V) and alpha factor extracted from the modulated signal. (From Koltchanov et al. [93], Figs. 1 and 3 right. Reproduced by permission of © 2005 The Institute of Electrical and Electronics Engineers)

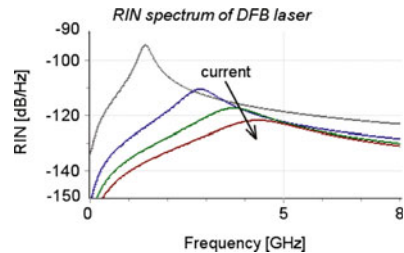
$$\alpha = 2I \frac{d\phi(t)/dt}{dI(t)/dt} \quad (2.35)$$

When operating the MZM with $\Delta\Phi_{\text{bias}} = \pi/4$ ideal intensity modulation is achieved for $\alpha = 0$. Traditionally MZMs are built on LiNbO_3 making use of the Pockels effect (linear dependence of the refractive index on the applied bias voltage). The progress in monolithic integration is supporting the development of InP-based integrated transmitters providing benefits such as lower voltage drive requirements, shorter device dimensions and the possibility to integrate with laser sources or optical amplifiers. InP modulators are based on the Kerr and Frank–Keldysh effect (bulk structures) or QCSE (multi-quantum well structures) so that the refractive index change is quadratic with voltage and the absorption change is linear with voltage [94]. The electro-refractive effect enables the development of MZMs with low voltage drive requirements and short electrode lengths. Using a phenomenological modeling approach for the electro-refraction affects the change of the group effective index of the guided optical mode Δn as described in Arellano et al. [89] as:

$$\Delta n = r_1 V + r_2 V^2 + \frac{dn}{dN} (N - N_0) \quad (2.36)$$

The first two terms on the right-hand side represent the electro-refractive index change that occurs due to electro-absorption. This may be caused by the Pockels and Kerr effects and it is described by the linear r_1 and quadratic r_2 change of refractive index with voltage V . The last term represents the carrier-dependent refractive index change. Here, dn/dN is the differential refractive index, N is the carrier density, and N_0 is the reference carrier density for which the chirp-induced frequency offset is zero.

Fig. 2.18 RIN spectrum of DFB laser for different drive currents



2.6.2 Transmitter-Induced Signal Degradation Effects

2.6.2.1 Laser Noise

Due to spontaneous emission taking place inside semiconductor lasers used for direct modulation or as optical light sources for external modulators, photons with random phase are added to the coherent output field which is generated by stimulated emission inside the laser, creating small perturbations of the amplitude and phase. Random variations of the laser intensity limit the maximum achievable OSNR while random variations of the phase lead to an increased spectral linewidth of the laser [8].

The relative intensity noise (RIN) describes the ratio of the mean-squared fluctuations in the observed PSD and the average output power of the laser [32]. The amount of RIN is independent of attenuation along a link as both the nominal signal power and the noise are attenuated equally. RIN represents a fundamental limit to the transmission capacity of high-speed links and the carrier-to-noise performance of analog links. For lasers in multimode operation mode partition noise (MPN) defines the RIN in a single mode relative to the RIN of all the modes. MPN represents an important measure for lasers emitting more than one mode (and this includes standard DFB lasers), since even if the overall RIN is small, individual modes may show large intensity fluctuations.

Using a simple system-level modeling approach, intensity noise could be approximated by a Gaussian random noise process and specified with respect to a given reference power. If the laser output power is different from that number then the RIN has to be scaled inversely to emulate the effect that the laser RIN scales inverse proportionally to the drive current (assuming the ratio of stimulated and spontaneous emission scales with drive current and the laser is not saturating). This model however, produces a flat electrical noise spectrum. Although this is rather unrealistic since RIN follows the intrinsic frequency response of the laser, this assumption can be used to emulate the worst-case impact of RIN. The RIN spectrum could be calculated more accurately using rate equations for modeling the laser characteristics [95]. The RIN spectrum of a DFB laser for four different drive currents is depicted in Fig. 2.18 showing clearly the dependence of the spectral RIN peak due to the carrier-photon resonance of the laser.

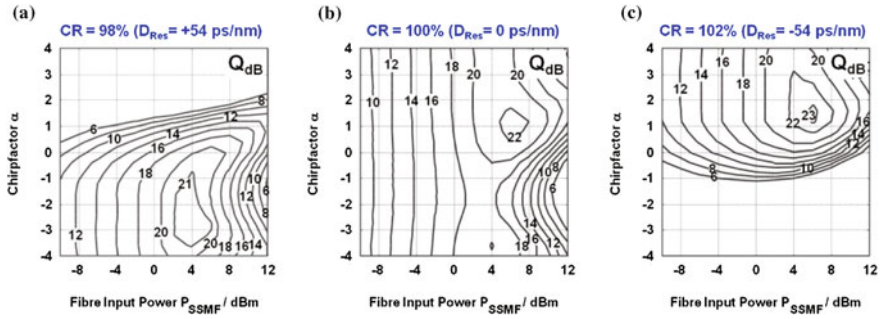


Fig. 2.19 Q factor versus transmitter pre-chirp and fiber input power for **a** under-compensated; **b** completely compensated; **c** over-compensated transmission sections for 40 Gbit/s NRZ over 2×80 km SSMF with one EDFA per section. (From Freund et al. [97], Fig. 4. Reproduced by permission of © 2004 The Institute of Electrical and Electronics Engineers)

The spectral linewidth of a laser is defined as the width (full-width at half-maximum, FWHM) of the CW spectrum which could be approximated by a Lorentzian shape (if correlation between intensity and phase fluctuations is neglected and relaxation oscillations are ignored) [8]. Typically the linewidth of DFB laser sources is below 20 MHz, and thus only of small importance for externally modulated systems utilizing direct-detection receivers since the modulation bandwidth is much wider (e.g., on the order of the driving symbol rate). However, phase fluctuations of optical sources with a linewidth in the MHz range could represent limitations for direct modulated systems as well as high-speed systems utilizing coherent reception. For the latter type of systems a more accurate modeling than the Lorentzian approximation of the spectral line shape is advisable (for details, see for instance [96]).

2.6.2.2 Chirp and Fiber Effects

As discussed in the previous sections, the interactions among transmitter chirp, fiber CD, and Kerr nonlinearities can have a strong impact on transmission system performance. Figure 2.19 shows sample simulation results of such interdependency. Contour plots of the Q factor are shown against fiber input power and transmitter chirp for a 40 Gbit/s NRZ transmission over two spans of 80 km SSMF for different degrees of dispersion compensation (compensation ratio, CR). Similar performance optima can be achieved for all dispersion maps for carefully selected values of the transmitter chirp. However, the system tolerance against chirp fluctuations varies significantly between completely compensated links (Fig. 2.19b) and links with under- or over-compensation (Fig. 2.19a, c). Consequently, when designing 40 Gbit/s WDM systems without exact compensation of the CD slope, each channel requires individual CD compensation depending on initial chirp and residual dispersion per channel.

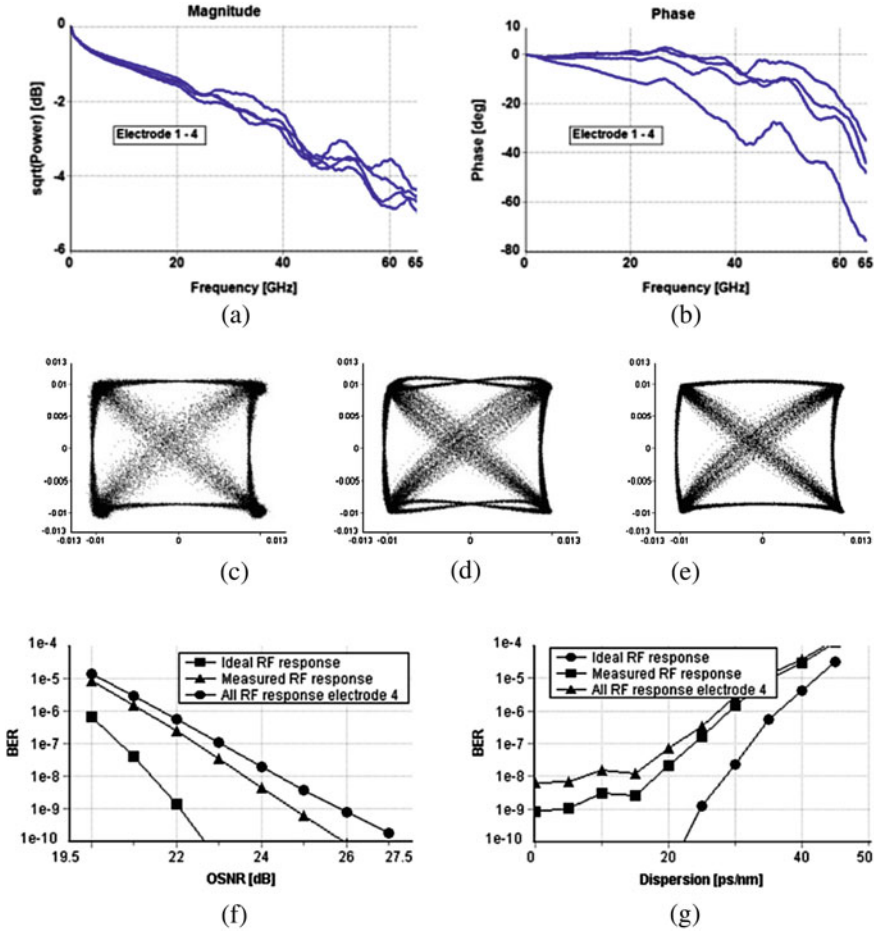


Fig. 2.20 a and b show S_{21} responses measured at input ports after smoothing; c Constellation diagrams of 80 Gbit/s DQPSK for an ideal S_{21} response; d measured magnitude and phase; e measured magnitude only; f BER of 80 Gbit/s DQPSK modulated signal versus OSNR; g BER of 80 Gbit/s DQPSK modulated signal versus residual CD for OSNR = 25 dB. (From Arellano et al. [100], Figs. 6, 7, and 8. Reproduced by permission of © 2009 The Institute of Electrical and Electronics Engineers)

2.6.2.3 Drivers and E/O-Contact Limitations

High-speed applications that need to manage large signal bandwidths show increased requirements on electrical components and electro-optical interconnects. At first, electrical drive circuits produce signals with an intrinsic amplitude noise, timing jitter, and imbalance between rise and fall times introducing restrictions to the ideal driving scenario of optical modulators. Furthermore, the optical

modulator bandwidth is restricted setting limits on the maximum driving speed. One of the main phenomena that limit the modulation bandwidth is the mismatch between microwave and optical velocities and frequency-dependent microwave attenuation [98]. Although it is possible to match microwave and optical refractive indices by electrode design techniques, the attenuation in the microwave driving circuit cannot be avoided and determines the frequency response of the device [99]. Typical MZM-based transmitters have an electrical bandwidth of up to 40 GHz. When designing, for instance, a 40 Gbit/s DQPSK transmission system using a modulator with 20 GHz electrical bandwidth, modeling of bandwidth limitations can be ignored as the modulator bandwidth is large enough to behave transparently on the data signal. However, driving the same device with double the bitrate, i.e. 40 Gbit/s in-phase and quadrature signals, electrical bandwidth limitations introduce a penalty, and thus have to be considered carefully in the design.

Results of a corresponding case study are depicted in Fig. 2.20 demonstrating that imbalanced frequency responses of the electrodes of an I-Q modulator may cause a significant penalty to the system performance, and thus are important to be considered in high-speed applications. Figure 2.20a, b show measured S_{21} responses (magnitude and phase) of the four MZMs. The constellation diagrams of an 80 Gbit/s DQPSK signal vary significantly when assuming ideal S_{21} responses (Fig. 2.20c), applying the measured S_{21} information (Fig. 2.20d), and when using the measured S_{21} magnitudes but assuming ideal phase responses (Fig. 2.20e). Consequently, the predictions of BER versus OSNR (Fig. 2.20f) and versus residual CD (Fig. 2.20 g) differ significantly with the applied model.

2.7 Conclusions

The above work introduced the reader into the concept of multiple optical signal representations and the major physical layer effects causing system degradations in the WDM transport layer. The focus was on deriving computer models for the various effects and for that matter these were grouped into categories such as fiber propagation, optical amplification, and transmitter-induced signal degradation effects. Within the fiber propagation category, effects were divided into linear, nonlinear, and polarization-dependent.

Suitable modeling approaches were presented, and typical simulation results were demonstrated.

Acknowledgment The author thanks Igor Koltchanov, Hadrien Louchet, Jim Farina, Cristina Arellano, and other (current and former) members of the team at VPIphotonics for sharing their invaluable knowledge and numerous contributions referenced in this work.

References

1. Lowery AJ, Lenzmann O, Koltchanov I, Moosburger R, Freund R, Richter A, Georgi S, Breuer D, Hamster H (2000) Multiple signal representation simulation of photonic devices, systems, and networks. *IEEE J Sel Top Quant Electron* 6(2):282–296
2. User's Manual (2010) VPItransmissionMaker™ Optical Systems, Version 8.5
3. Piprek J (ed) (2003) Optoelectronic devices: advanced simulation and analysis. Springer, New York
4. Richter A, Louchet H, Koltchanov I (2007) Pitfalls when modeling high-speed optical transmission systems. In: *Proceedings of IEEE/LEOS Summer Topicals*, paper TuE1.1, Portland, OR, pp 238–239
5. Gowar J (1984) Optical communication systems. Prentice Hall, Englewood Cliffs, pp 71–80
6. Keiser G (2000) Optical fiber communications, 3rd edn. McGraw-Hill, Boston
7. Chraplyvy A (1990) Limitations on lightwave communications imposed by optical-fiber nonlinearities. *IEEE/OSA J Lightwave Technol* 8(10):1548–1557
8. Agrawal GP (2002) Fiber-optic communication systems, 3rd edn. Wiley Inter-science, New York
9. Agrawal GP (1995) Nonlinear fiber optics, 3rd edn. Academic Press, New York
10. Kato T, Koyano Y, Nishimura M (2000) Temperature dependence of chromatic dispersion in various types of optical fiber. *Opt Lett* 25(16):1156–1158
11. Liu F et al. (2002) 1.6Tbit/s (40x42.7 Gbit/s) transmission over 3600 km ultra wave fiber with all-Raman amplified 100 km terrestrial spans using ETDM transmitter and receiver. In: *Proceedings of IEEE/OSA optical fiber communication conference (OFC)*, post-deadline paper FC7, Anaheim, CA
12. Inoue K (1992) Four-wave mixing in an optical fiber in the zero-dispersion wavelength region. *IEEE/OSA J Lightwave Technol* 10(11):1553–1561
13. Oppenheim AV, Schaffer RW (1989) Discrete-time signal processing. Prentice Hall, Englewood Cliffs, pp 587–622
14. Mecozzi A, Clausen CB, Shtaif M (2000) Analysis of intrachannel nonlinear effects in highly dispersed optical pulse transmission. *IEEE Photonics Technol Lett* 12(4):392–394
15. Essiambre RJ, Mikkelsen B, Raybon G (1999) Intra-channel cross-phase modulation and four-wave mixing in high-speed TDM systems. *Electron Lett* 35(18):1576–1578
16. Mamyshev PV, Mamysheva NA (1999) Pulse-overlapped dispersion-managed data transmission and intrachannel four-wave mixing. *Opt Lett* 24(21):1454–1456
17. Clausen CB, Mecozzi A, Shtaif M (2000) Nonlinear intra-channel effects: system impairments and their remedy. In: *Proceedings of European conference on optical communications (ECOC)*, vol 3, Munich, Germany, pp 33–34
18. Martensson J, Westlund M, Berntson A (2000) Intra-channel pulse interactions in 40 Gbit/s dispersion-managed RZ transmission. *Electron Lett* 36(3):244–246
19. Killey RI, Thiele HJ, Mikhailov V, Bayvel P (2000) Reduction of intrachannel nonlinear distortion in 40 Gb/s-based WDM transmission over standard fiber. *IEEE Photonics Technol Lett* 12(12):1624–1626
20. Richter A (2002) Timing jitter in long-haul WDM return-to-zero systems. Dissertation, Technische Universität Berlin, Germany
21. Breuer D, Schneider M, Vorbeck S, Freund R, Richter A (2004) Design analysis of upgrade strategies from single to double and triple-wavelength-band WDM transmission. In: *Proceedings of IEEE Asia-Pacific optical communications conference (APOC)*, vol 5625, Beijing, China, pp 601–613
22. Kidorf H, Rottwitt K, Nissov M, Ma M, Rabarjaona E (1999) Pump interactions in a 100-nm bandwidth Raman amplifier. *IEEE Photonics Technol Lett* 11(5):530–532
23. Namiki S, Emori Y (2001) Ultrabroad-band Raman amplifiers pumped and gain-equalized by wavelength-division-multiplexed high-power laser diodes. *IEEE J Sel Top Quant Electron* 7(1):3–16

24. Kaminow IP, Li T (eds) (2002) Optical fiber telecommunications IVB: systems and impairments. Academic Press, San Diego, CA
25. Iannone E, Matera F, Mecozzi A, Settembre M (1998) Nonlinear optical communication networks. Wiley, New York
26. Gordon JP, Kogelnik H (2000) PMD fundamentals: polarization mode dispersion in optical fibers. *PNAS* 97(9):4541–4550
27. Wai PKA, Menyuk CR (1996) Polarization mode dispersion, decorrelation, and diffusion in optical fibers with randomly varying birefringence. *IEEE/OSA J Lightwave Technol* 14(2):148–157
28. Curti F, Daino B, de Marchis G, Matera F (1990) Statistical treatment of the evolution of the principal states of polarization in single-mode fibers. *IEEE/OSA J Lightwave Technol* 8(8):1162–1166
29. Collett E (1993) Polarized light: fundamentals and applications. Marcel Dekker, New York
30. Foschini GJ, Pole CD (1991) Statistical theory of polarization dispersion in single-mode fibers. *IEEE/OSA J Lightwave Technol* 9(11):1439–1456
31. Freund R, Molle L, Hanik N, Richter A (2004) Design issues of 40-Gbit/s WDM systems for metro and core network application. In: Proceedings of IEEE Asia-Pacific optical communications conference (APOC), vol 5625, Beijing, China, pp 532–543
32. Derrickson D (1998) Fiber optic test and measurement. Prentice Hall, Upper Saddle River
33. Mecozzi A, Shtaif A (2002) The statistics of polarization-dependent loss in optical communication systems. *IEEE Photonics Technol Lett* 14(3):313–315
34. Gisin N, Huttner B (1997) Combined effects of polarization mode dispersion and polarization dependent losses in optical fibers. *Opt Commun* 142(1–3):119–125
35. Steinkamp A, Vorbeck S, Voges E (2004) Polarization mode dispersion and polarization dependent loss in optical fiber systems. In: Proceedings of SPIE Optics East, vol 5596, Philadelphia, PA, pp 243–254
36. Antoniadis N, Reichmann KC, Iannone PP, Frigo NJ, Levine AM, Roudas I (2006) The impact of polarization-dependent gain on the design of cascaded semiconductor optical amplifier CWDM systems. *IEEE Photonics Technol Lett* 18(20):2099–2101
37. Lee M, Antoniadis N, Boskovic A (2002) PDL-induced channel power divergence in a metro WDM network. *IEEE Photonics Technol Lett* 14(4):561–563
38. Wang D, Menyuk CR (1999) Polarization evolution due to the Kerr nonlinearity and chromatic dispersion. *IEEE/OSA J Lightwave Technol* 17(12):2520–2529
39. Hodzic A, Konrad B, Petermann K (2003) Improvement of system performance in Nx40-Gb/s WDM transmission using alternate polarizations. *IEEE Photonics Technol Lett* 15(1):153–155
40. Forzati M, Berntson A, Martensson J (2004) IFWM suppression using APRZ with optimized phase-modulation parameters. *IEEE Photonics Technol Lett* 16(10):2368–2370
41. Richter A, Koltchanov I, Lowery A (2004) Photonic design automation of optical communication systems. In: Proceedings of IEEE Asia-Pacific optical communications conference (APOC), vol 5625, Beijing, China, pp 316–327
42. Bosco G, Carena A, Curri V, Gaudino R, Poggiolini P, Benedetto S (2000) Suppression of spurious tones induced by the split-step method in fiber systems simulation. *IEEE Photonics Technol Lett* 12(5):489–491
43. Rasmussen CJ (2001) Simple and fast method for step size determination in computations of signal propagation through nonlinear fibers. In: Proceedings of IEEE/OSA optical fiber communication conference (OFC), paper WDD29-1, Anaheim, CA
44. Taha TR, Ablowitz MJ (1984) Analytical and numerical aspects of certain nonlinear evolution equations. II. numerical, nonlinear Schroedinger equation. *J Comput Phys* 55(2):203–230
45. Carena A, Curri V, Gaudino R, Poggiolini P, Benedetto S (1997) A time-domain optical transmission system simulation package accounting for nonlinear and polarization-related effects in fibers. *IEEE J Sel Areas Commun* 15(4):751–765
46. Brigham EO (1974) The fast fourier-transform. Prentice-Hall, Englewood Cliffs

47. Singleton RC (1967) A method for computing the fast Fourier transform with auxiliary memory and limited high-speed storage. *IEEE Trans Audio Electroacoustics* 15(2):91–98
48. Yu T, Reimer WM, Grigoryan VS, Menyuk CR (2000) A mean field approach for simulating wavelength-division multiplexed systems. *IEEE Photonics Technol Lett* 12(4):443–445
49. Wai PKA, Menyuk CR, Chen HH (1991) Stability of solitons in randomly varying birefringent fibers. *Opt Lett* 16(16):1231–1233
50. Marcuse D, Menyuk CR, Wai PKA (1997) Application of the Manakov-PMD equation to studies of signal propagation in optical fibers with randomly varying birefringence. *IEEE/OSA J Lightwave Technol* 15(9):1735–1746
51. Biondini G, Kath WL, Menyuk CR (2002) Importance sampling for polarization-mode dispersion. *IEEE Photonics Technol Lett* 14(3):310–312
52. Menyuk CR (1987) Nonlinear pulse propagation in birefringence optical fibers. *IEEE J Quant Electron* 23(2):174–176
53. Nelson LE, Jopson R (2002) Introduction to polarization mode dispersion in lightwave systems Venice Summer School on PMD, Venice, Italy, pp 24–26
54. Shtaif M, Mecozzi A (2000) Study of the frequency autocorrelation of the differential group delay in fibers with polarization mode dispersion. *Opt Lett* 25(10):707–709
55. Richter A, Dazert M, Koltchanov I, Myslivets E, Lowery A (2002) Performance degradations in high-speed (40 Gbit/s +) transmission systems due to polarization mode dispersion. In: *Proceedings of IEEE/OSA national fiber optics engineers conference (NFOEC)*, paper 073, Anaheim, CA
56. Richter A, Koltchanov I, Kuzmin K, Myslivets E, Freund R (2005) Issues on bit-error rate estimation for fiber-optic communication systems. In: *Proceedings of IEEE/OSA optical fiber communication conference (OFC/NFOEC)*, paper NTuH3, Anaheim, CA
57. Richter A, Koltchanov I, Kuzmin K, Rukhlenko D (2005) Bit-error rate estimation for applications using 40 Gbit/s and higher. In: *Proceedings of IEEE workshop on optical transmission and equalization (WOTE)*, paper B3, Shanghai, China, pp 23–24
58. Francia C, Bruyere F, Penninckx D, Chbat M (1998) PMD second-order effects on pulse propagation in single-mode optical fibers. *IEEE Photonics Technol Lett* 10(12):1739–1741
59. Kogelnik H, Nelson LE, Gordon JP, Jopson RM (2000) Jones matrix for second-order polarization mode dispersion. *Opt Lett* 25(1):19–21
60. Eyal A, Marshall WK, Tur M, Yariv A (1999) Representation of second-order polarization mode dispersion. *IEEE Electron Lett* 35(19):1658–1659
61. Orlandini A, Vincetti L (2001) A simple and useful model for Jones matrix to evaluate higher order polarization-mode dispersion effects. *IEEE Photonics Technol Lett* 13(11):1176–1178
62. Poloyko I, Khilo A, Myslivets E, Volkov V, Koltchanov I, Richter A, Lowery A (2003) Photonic design automation of Raman amplified systems. In: *Proceedings of IEEE/OSA national fiber optics engineers conference (NFOEC)*, paper P29, Atlanta, GA
63. Photonic Modules Reference Manual (2011) VPItransmissionMakerTM Optical Systems, Version 8.6
64. Rottwitz K, Bromage J, Leng L (2002) Scaling the Raman gain coefficient of optical fibers. In: *Proceedings of European conference on optical communications (ECOC)*, paper S3.03, Copenhagen, Denmark
65. Grant AR (2002) Calculating the Raman pump distribution to achieve minimum gain ripple. *IEEE J Quant Electron* 38(11):1503–1509
66. Perlin VE, Wintful HG (2002) On distributed Raman amplification for ultrabroad-band long-haul WDM systems. *IEEE/OSA J Lightwave Technol* 20(3):409–416
67. Richter A, Koltchanov I, Myslivets E, Khilo A, Shkred G, Freund R (2005) Optimization of multi-pump Raman amplifiers. In: *Proceedings of IEEE/OSA optical fiber communication conference (OFC/NFOEC)*, paper NTuB4, Anaheim, CA
68. Lin Q, Agrawal G (2003) PMD effects in fiber-based Raman amplifiers. In: *Proceedings of IEEE/OSA optical fiber communication conference (OFC)*, paper TuC4, Atlanta, GA

69. Richter A, Louchet H, Poloyko I, Karelin N, Farina J, Koltchanov I (2009) A parametric approach to optical systems design, optimization and validation. In: Proceedings of European conference on networks and optical communications (NOC), Valladolid, Spain, pp 361–367
70. Mears RJ, Reekie L, Jauncey IM, Payne DN (1987) Low noise erbium doped fiber amplifier operating at 1.54 μm . *IEEE Electron Lett* 23(19):1026–1028
71. Desurvire E (1994) Erbium-doped fiber amplifiers, principles and applications. Wiley, New York
72. Becker PC, Olsson NA, Simpson JR (1999) Erbium-doped fiber amplifiers, fundamentals and technology. Academic Press, New York
73. Giles R, Desurvire E (1991) Modeling erbium-doped fiber amplifiers. *IEEE/OSA J Lightwave Technol* 9(2):271–283
74. User's Manual (2011) VPIcomponentMakerTM Optical Amplifiers, Version 8.6
75. Abramovich F, Bayvel P (1997) Some statistical remarks on the derivation of BER in amplified optical communication systems. *IEEE Trans Commun* 45(9):1032–1034
76. Keiser G (2000) Optical fiber communications, 3rd edn. McGraw-Hill, Boston
77. Collin RE (1992) Foundations for microwave engineering, 2nd edn. McGraw-Hill, New York
78. Bonnedal D (1996) EDFA gain described with a black box model. In: Proceedings of OSA trends in optics and photonics, optical amplifiers and their applications, vol 5, Washington, D.C., pp 53–56
79. Burgmeier J, Cords A, März R, Schäffer C, Stummer B (1998) A black box model of EDFA's operating in WDM systems. *IEEE/OSA J Lightwave Technol* 16(7):1271–1275
80. Zhang X, Mitchell A (2000) A simple black box model for erbium-doped fiber amplifiers. *IEEE Photonics Technol Lett* 12(1):28–30
81. Jacobsen G, Persson U, Gillner L, Vanin E, Wingstrand S (2000) Pump power dependent black box EDFA model. *J Opt Commun* 21(5):171–177
82. Villa JAL, Bo FB, Querol VP, Teixeira AL, Prat Goma J (2008) Extended black box model for fiber length variation of erbium-doped fiber amplifiers. *IEEE Photonics Technol Lett* 20(24):2063–2065
83. Richter A, Devatine R, Koltchanov I, Lowery A, Khomchenko D, Yevseyenko D, Moar P (2002) Virtual product prototyping of erbium doped fiber amplifiers for applications in dense WDM systems. In: Proceedings of IEEE/OSA national fiber optics engineers conference (NFOEC), paper 153, Anaheim, CA
84. Yoo SJB, Xin W, Garratt LD, Young JC, Ellinas G, Chiao JC, Rauch M, Baran JE, Meagher B, Leblanc H, Chang G-K (1998) Observation of prolonged power transients in a reconfigurable multiwavelength network and their suppression by gain-clamping of optical amplifiers. *IEEE Photonics Technol Lett* 10(11):1659–1661
85. Richter A, Karelin N, Louchet H, Koltchanov I, Farina J (2010) Dynamic events in optical networks—emulation and performance impact analysis. In: Proceedings of IEEE military communication conference (MILCOM), San Jose, CA, pp 1083–1087
86. Matsui Y, Mahgerefteh D, Zheng X, Liao C, Fan ZF, McCallion K, Tayebati P (2006) Chirp-managed directly modulated laser (CML). *IEEE Photonics Technol Lett* 18(2):385–387
87. Cartledge JC, Srinivasan RC (1997) Extraction of DFB laser rate equation parameters for system simulation purposes. *IEEE/OSA J Lightwave Technol* 15(5):852–860
88. Lowery AJ (1992) A two-port bilateral model for semiconductor lasers. *IEEE J Quant Electron* 28(1):82–92
89. Arellano C, Mingaleev S, Novitsky A, Koltchanov I, Richter A (2009) Design of complex semiconductor integrated structures. In: Proceedings of IEEE Asia communication and photon conference (ACP) 7631, paper 7631-106, Shanghai, China
90. Gnauck AH, Korotky SK, Veselka J, Nagal J, Kemmner CT, Mindford WJ, Moser DT (1991) Dispersion penalty reduction using an optical modulator with adjustable chirp. *IEEE Photonics Technol Lett* 3(10):916–918

91. Hashimoto JI, Nakano Y, Tada K (1992) Influence of facet reflection on the performance of a DFB laser integrated with an optical amplifier/modulator. *IEEE J Quant Electron* 28(3):594–603
92. Koyama F, Iga K (1998) Frequency chirping in external modulators. *IEEE/OSA J Lightwave Technol* 6(1):87–93
93. Koltchanov I, Richter A, Myslivets E, Kazmierski C (2005) Complete time and frequency-dependent modeling of electro-absorption modulators. In: *Proceedings of IEEE/OSA optical fiber communication conference (OFC/NFOEC)*, paper OME42, Anaheim, CA
94. Mendoza-Alvarez JG, Coldren LA, Alping A, Yan RH, Hausken T, Lee K, Pedrotin K (1988) Analysis of depletion edge translation lightwave modulators. *IEEE/OSA J Lightwave Technol* 6(6):793–808
95. Ahmed M, Yamada M, Saito M (2001) Numerical modeling of intensity and phase noise in semiconductor lasers. *IEEE J Quant Electron* 37(12):1600–1610
96. Betti S, De Marchis G, Iannone E (1995) *Coherent optical communication systems*. Wiley Inter-science, New York
97. Freund R, Molle L, Hanik N, Richter A (2004) Design issues of 40 Gbit/s WDM-systems for metro and core network application. In: *Proceedings of European conference on optical communications (ECOC)*, paper Tu351, Stockholm, Sweden
98. Kaminow IP, Koch TL (eds) (1997) *Optical fiber telecommunications IIIB*. Academic Press, San Diego, CA
99. Dutta AK, Dutta NK, Fujiwara M (eds) (2002) *WDM technologies: active optical components*. Academic Press, New York
100. Arellano C, Louchet H, Koltchanov I, Richter A (2009) Important device limitations of transmitter and receiver concepts when designing 100 G transmission systems. In: *Proceedings of IEEE international conference on transparent optical networks (ICTON)*, paper Tu.C2.3, Azores, Portugal

WDM Systems and Networks

Modeling, Simulation, Design and Engineering

Antoniades, N.N.; Ellinas, G.; Roudas, I. (Eds.)

2012, XVI, 532 p., Hardcover

ISBN: 978-1-4614-1092-8